White Rose Research Online
eprints@whiterose.ac.uk
https://eprints.whiterose.ac.uk
Universities of Leeds, Sheffield and York

Deposited via The University of Leeds.

White Rose Research Online URL for this paper:
https://eprints.whiterose.ac.uk/id/eprint/236518/

Article:

Lu, Y., Gidel, F., Bunnik, T. et al. (Accepted: 2026) Variationally and numerically coupled water-wave and surf-zone hydrodynamics. Journal of Engineering Mathematics. ISSN: 0022-0833 (In Press)

This is an author produced version of an article accepted for publication in Journal of Engineering Mathematics, made available via the University of Leeds Research Outputs Policy under the terms of the Creative Commons Attribution License (CC-BY), which permits unrestricted use, distribution and reproduction in any medium, provided the original work is properly cited.

Reuse

Items deposited in White Rose Research Online are protected by copyright, with all rights reserved unless indicated otherwise. They may be downloaded and/or printed for private study, or other acts as permitted by national copyright laws. The publisher or other rights holders may allow further reproduction and re-use of the full text version. This is indicated by the licence information on the White Rose Research Online record for the item.

Takedown

If you consider content in White Rose Research Online to be in breach of UK law, please notify us by emailing eprints@whiterose.ac.uk including the URL of the record and the reason for the withdrawal request.

UNIVERSITY OF LEEDS
University of Sheffield
UNIVERSITY of York

Journal of Engineering Mathematics (2026) 157:2
https://doi.org/10.1007/s10665-026-10511-9

Variationally and numerically coupled water-wave and surf zone hydrodynamics

Yang Lu[1] · **Floriane Gidel**[2] · **Tim Bunnik**[3] · **Onno Bokhove**[1] · **Mark Kelmanson**[1]

Received: 21 August 2025 / Accepted: 13 January 2026 / Published online: 25 February 2026

Abstract

To improve the cost-effectiveness of modelling of wave interactions, a "numerical wavetank" is presented whose distinctive novel feature is its ability to couple both deep-water potential-flow and shallow-water models to controllable, prespecified wavemaker motion and beach topography. The coupling is in part obtained via a variational principle approach that guarantees important conservation properties and numerical stability. The model presented is the first fully nonlinear model to couple deep-water (discretised as finite elements) and shallow-water equations (discretised as finite volumes). Resulting simulations of wave generation, propagation and absorption by shallow-water-wave breaking are presented and analysed. A discussion is given on the efficacy of the novel approach.

Keywords Compatible finite-element method · Finite-volume shallow-water method · Potential-flow water-wave dynamics · Shallow-water surf zone · Variationally coupled dynamics

---

Yang Lu and Floriane Gidel have contributed equally to this work.

✉ Onno Bokhove
o.bokhove@leeds.ac.uk

Yang Lu
mmyl@leeds.ac.uk

Floriane Gidel
floriane.gidel@gmail.com

Tim Bunnik
t.bunnik@marin.nl

Mark Kelmanson
markkelmanson@gmail.com

[1] School of Mathematics, University of Leeds, Woodhouse Lane, LS2 9JT Leeds, Yorkshire, UK

[2] SOPHiA GENETICS, Bidart, France

[3] Research and Development, Maritime Research Institute Netherlands, Haagsteeg 2, 6708PM Wageningen, Gelderland, The Netherlands

1 Introduction

Rogue (also called freak) waves have been feared throughout history, ever since scientists have begun to understand them. Despite having for centuries traumatised and even killed mariners, suddenly appearing huge waves at sea started to raise scientific attention only as late as the end of the twentieth century, during which several instances of severe ship damage and losses of strong vessels offered evidence that increased both the credibility of mariners and the curiosity of scientists. On January 1st 1995, a 25.6m-high wave measured at the Draupner offshore platform was 2.25 times higher than all previously recorded averaged wave heights in the North Sea area [1]: this "New Year wave" not only proved beyond dispute the existence of such extreme and sudden waves but also catalysed research into rogue waves, on which a thorough overview of current knowledge is given in [2].

It is timely from an environmentalist perspective to focus on such threatening and unpredictable rogue waves since they are expected to occur with increasing frequency due to global warming [3, 4]. The clear motivation for such focus is to ameliorate the safety of crews and passengers using a combination of mathematical modelling, numerical methods and experiments to inform the design of maritime structures that are able to resist extreme events. Experimental scaled-down rigs in the form of wave tanks are already used by the maritime industry, e.g. at the Maritime Research Institute of the Netherlands (MARIN), for research on rogue-wave impact on offshore structures. These rigs often consist of basins with controllable-speed wavemakers on one or two sides, and beaches to dampen the waves on the remaining sides. But such wavetank tests are quite expensive so, to increase their efficacy, presented and exemplified herein is a "numerical wavetank" that is able to simulate water-wave dynamics in a finite experimental basin. Creating such a numerical wavetank is challenging on three fronts: first, the wavemaker motion must be captured; second, dispersive and nonlinear intermediate-depth to deep-water-wave dynamics must be modelled; and, third, breaking-wave dynamics in the beach surf zone must be captured.

To address the first two challenges, we have developed mathematical and numerical strategies to model nonlinear intermediate-depth and deep-water waves, driven by a wavemaker, using a compatible, variational discretisation of a nonlinear potential-flow water-wave model [5–7]. Our models are able to simulate cost-effectively the propagation of freak waves [6, 8], which constitute a significant hazard to offshore structures. Moreover, the numerical model may be used to simulate 2D and 3D waves generated by a piston wavemaker, and can be used to optimise experimental set-ups in wave tanks used by the maritime industry. To address the third aspect, an absorbing boundary condition in the form of the shallow-water beach used in actual experimental wavetanks-instead of rigid, vertical walls—is implemented here. The aim is to reduce the length of the numerical domain to the target area without disturbing the wave-structure-interaction tests with reflected waves that would be absent in a real sea state.

Various absorbing boundary methods already exist to dampen water waves: a commonly used technique is the implementation of a relaxation zone, also called "forcing/damping zone" or "absorbing layer", in which an analytical solution of the equations is used to compute reflection coefficients and to absorb the incoming waves.

This method was implemented in, e.g. the open-source library Open-Foam [9] by Jacobsen et al. [10], who define the relaxation zone depending on wavelength and geometry of the computational domain. However, the methods provided to compute reflection factors are efficient mainly in the shallow-water regime, whereas our numerical wavetank also aims to generate intermediate-to-deep-water waves. Although Peric and Maksoud [11, 12] introduced extended methods to estimate reflection coefficients to prime simulations, thereby obtaining results efficiently for deep-water waves, their relaxation method is, however, efficient only when an analytical solution may be estimated, typically for regular waves; it is not yet applicable to irregular waves that cannot be predicted *a priori*. Our numerical tank will be used to simulate irregular sea states with unknown wave profiles at the boundary, for which configuration the relaxation method in [11, 12] cannot be applied. Duz et al. [13] provided a solution for the absorption of both regular and irregular waves based on the boundary operator initially introduced by Higdon [14, 15]. The extended boundary operator, computed from the dispersion relation for the solution of the Laplace equation and based on the angle of incidence of the generated waves, is applied on the boundary of the numerical domain through ghost cells beyond the mesh periphery in the Volume-Of-Fluid numerical method. Whilst comparison with reference solutions showed relatively good agreement in absorbing the waves, the second-order absorbing boundary condition introduced in [16] showed much improved wave absorption. This extended boundary, second-order Higdon operator accounted for not only dispersive but also directional wave effects. Such operators, obtained from linear wave theory and linearized Bernouilli equations augmented by second-order weakly nonlinear corrections, are, however, not applicable to steep nonlinear waves such as freak waves.

Alternatively, wave-breaking parametrization schemes have been successfully applied to Boussinesq as well as potential-flow models, such as the parameterisations developed by Smit et al. [17] and Wang et al. [18], based on either shallow-water celerity or wave steepness considerations. Instead, as a complementary approach, our goal is to numerically couple a potential-flow model to a shallow-water model with wave breaking in the surf zone, given the wave absorption characteristics of the beach in the laboratory wave basin. Whilst these wave-breaking parameterisations involve phenomenological criteria signalling where local dissipation is applied in additional dissipative terms, the classical shallow-water equations in hyperbolic conservative form intrinsically trigger energy dissipation where shock or bore formation occurs as proxy for wave breaking. The challenge herein is the coupling of two different mathematical and numerical modelling approaches into a unified numerical model.

The first step in responding to demands placed upon the maritime industry is to configure model tests of wave–structure interactions in experimental wave basins. In the configuration used herein, water waves are dampened at a beach, thereby offering wave absorption through shallow-water-wave breaking at the beach. This allows design of a numerical tank that emulates the performance of in-house experimental rigs (e.g. at the Maritime Research Institute Netherlands—MARIN). Close to the wave-breaking swash zone, the potential-flow model is invalid, and it yields an unstable associated finite-element method. Instead, we choose to model beach dynamics locally by the

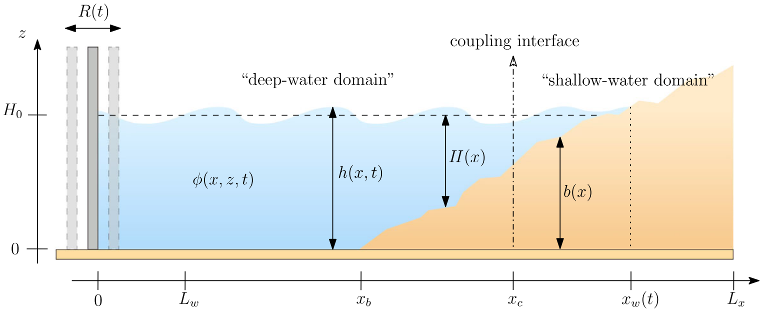

Fig. 1 Schematic of the two-dimensional wavetank, with a piston wavemaker on the left-hand boundary and a beach on the opposite boundary. Two subdomains divide the basin: a deep-water domain, where nonlinear potential-flow equations are solved, and a shallow-water surf zone, where nonlinear shallow-water equations are applied. Coupling conditions are derived and implemented at the interface $x = x_c$ between these domains

nonlinear shallow-water equations, and solve these numerically with a classical finite-volume method. These equations describe non-dispersive waves with wave breaking included as hydraulic bores, as in Kristina et al. [19], whilst ensuring non-negative depth at the beach through Audusse et al.'s method [20].

Whilst previous studies have led to stable coupling between deep- and shallow-water equations (see [19] for linear Boussinesq equations coupled to nonlinear shallow-water equations, and [21] for linear potential flow coupled to nonlinear shallow-water equations), the model presented here is the first fully nonlinear model to couple deep- and shallow-water equations.

The paper outline is as follows: The variational continuum strategy is described in Sect. 2. Nonlinear coupling implementation strategies are described in Sect. 3. Resulting simulations of wave generation, wave propagation, and wave absorption are presented and analysed in Sect. 4. Conclusions on the efficiency of the present nonlinear numerical tank are discussed in Sect. 5, including a discussion of several recently discovered shortcomings of the model developed.

2 Variational coupling of deep- and shallow-water potential-flow models

2.1 Domain setup and coupling strategy

In this section, we present the mathematical model for the wavetank containing a surf zone, as illustrated in Fig. 1. The model simulates wave propagation in the x-direction within a two-dimensional (2D) vertical wave basin, with a time-dependent wavemaker driving wave motion at one end and a beach at the opposite end to dampen wave energy. The depth at rest is given by $H(x) = H_0 - b(x)$, where the beach topography begins at x_b. The rest depth is a constant H_0 for $x \leq x_b$ and decreases along the beach for $x \geq x_B$ until reaching zero at the moving waterline, $x = x_w(t)$. For $t > 0$, the piston wavemaker oscillates near the tank end at $x = 0$, and its motion is denoted by

$x = R(t)$. The wavemaker motion induces a surface displacement $\eta(x,t)$ from rest depth $H(x)$, resulting in a total water depth $h(x,t) = H(x) + \eta(x,t)$.

Figure 1 depicts the two-dimensional vertical domain, divided into two subdomains. In the first, the "deep-water domain" wave dynamics are resolved using the nonlinear potential-flow model developed in [5–7]. This time-dependent domain is defined as

$$\Omega_D = \{R(t) \le x < x_c;\ b(x) \le z \le b(x) + h(x,t)\}, \tag{1}$$

with the piston wavemaker prescribing the left-hand boundary at $x = R(t)$, the seabed topography forming the lower boundary $z = b(x)$. As waves propagate along the beach and enter the "shallow-water domain", defined by

$$\Omega_S = \{x_c < x \le x_w(t)\}, \tag{2}$$

the influence of the sloping seabed becomes dominant, modifying wave profiles and ultimately causing wave breaking. Due to the steep gradients associated with wave breaking in the surf zone, the phenomenon is treated as discontinuous, which presents challenges for classical continuous finite-element methods. These methods, whilst suitable for the deep-water regime, may produce numerical instabilities in regions with sharp gradients or discontinuities. Instead, wave motions in the shallow-water domain are described by the nonlinear shallow-water equations, which capture breaking as hydraulic bores (see [19]). Numerically, a well-balanced scheme is used to ensure non-negative water depth at the beach (see [20]). The two subdomains are linked via a coupling interface at Γ_c: $x = x_c$. Here, the deep- and shallow-water models—each discretised using numerical methods suited to their respective regimes—are coupled through carefully derived conditions. The coupling point x_c is chosen such that the local water depth $h(x_c)$ lies between the typical deep-water and shallow-water limits, specifically $h \ge \lambda/2$ and $h \le \lambda/20$, where λ is a representative wavelength of the waves under consideration. The coupling conditions between the potential-flow and shallow-water models are derived via a variational principle, as detailed in the next section.

2.2 Variational principle for the coupled domain

The aim is to understand and to simulate the dynamics occurring in Ω_D and Ω_S, including their dynamic coupling at $x = x_c$. The evolution of the water depth $h(x,t)$ and velocity potential $\phi(x,z,t)$ in the numerical basin shown in Fig. 1 is described by Luke's variational principle [22] for nonlinear waves

$$0 = \delta \int_0^T \int_{R(t)}^{x_w(t)} \int_{b(x)}^{b(x)+h(x,t)} \left[\partial_t \phi + \frac{1}{2}|\nabla \phi|^2 + g\,(z - H_0) \right] \mathrm{d}z\, \mathrm{d}x\, \mathrm{d}t. \tag{3}$$

Following the coupling strategy, the whole domain is partitioned into Ω_D and Ω_S, connected at the interface Γ_c located at $x = x_c$. Accordingly, the variational principle

(3) is decomposed into contributions from each subdomain:

$$
\begin{aligned}
0 = \delta \int_0^T \Bigg\{ &\int_{\Omega_D} \left[\partial_t \phi + \frac{1}{2} |\nabla \phi|^2 + g\,(z - H_0) \right] \mathrm{d}x\, \mathrm{d}z \\
&+ \int_{\Omega_S} \left[h \partial_t \check{\phi} + \frac{1}{2} h (\partial_x \check{\phi})^2 + g h \Big(\frac{1}{2} h - H \Big) \right] \mathrm{d}x \Bigg\} \,\mathrm{d}t,
\end{aligned}
\tag{4}
$$

where the velocity potential has been depth-averaged in Ω_S using the additional simplification

$$
\check{\phi}(x,t) = \frac{1}{h} \int_b^{b+h} \phi(x,z,t)\, \mathrm{d}z. \tag{5}
$$

Taking variations of the variational principle (4) with respect to h, ϕ, and $\check{\phi}$, and imposing temporal endpoint conditions $\delta\phi(0) = \delta\phi(T) = 0$ and $\delta\check{\phi}(0) = \delta\check{\phi}(T) = 0$, we obtain

$$
\begin{aligned}
0 = \int_0^T \Bigg\{ &\int_{R(t)}^{x_c} \Bigg[\int_b^{b+h} \delta\phi \big(-\partial_{xx}\phi - \partial_{zz}\phi \big)\, \mathrm{d}z - \delta\phi \Big(\partial_x \phi\, b_x - \partial_z \phi \Big)_{z=b} \\
&\quad + \delta h \Big(g(h - H) + \partial_t \phi + \frac{1}{2} |\nabla\phi|^2 \Big)_{z=b+h} \\
&\quad + \delta\phi \Big(-\partial_t h - \partial_x (h+b)\, \partial_x \phi + \partial_z \phi \Big)_{z=b+h} \Bigg] \mathrm{d}x \\
&+ \int_{x_c}^{x_w(t)} \Bigg[\delta h \Big(\partial_t \check{\phi} + \frac{1}{2} (\partial_x \check{\phi})^2 + g(h - H) \Big) \\
&\quad + \delta\check{\phi} \Big(-\partial_t h - \partial_x \check{\phi}\, \partial_x h - h \partial_{xx} \check{\phi} \Big) \Bigg] \mathrm{d}x \\
&+ \left[\int_b^{b+h} \delta\phi \big(\dot{R} - \partial_x \phi \big)\, \mathrm{d}z \right]_{x=R} + \left[\delta\check{\phi} \Big(h \partial_x \check{\phi} - h \dot{x}_w \Big) \right]_{x=x_W} \\
&+ \left[\int_b^{b+h} \delta\phi\, (\partial_x \phi)\, \mathrm{d}z \right]_{x=x_c} - \left[\delta\check{\phi} \Big(h \partial_x \check{\phi} \Big) \right]_{x=x_c} \\
&+ \left[\delta x_w \Big(h \partial_t \check{\phi} + \frac{1}{2} h (\partial_x \check{\phi})^2 + g h \Big(\frac{1}{2} h - H \Big) \Big) \right]_{x=x_w} \Bigg\} \,\mathrm{d}t,
\end{aligned}
\tag{6}
$$

where a dot denotes temporal differentiation, e.g. $\dot{R} = \mathrm{d}R/\mathrm{d}t$ and $b_x = \mathrm{d}b/\mathrm{d}x$.

By definition, the water depth at the waterline $x = x_w$ is $h(x_w, t) = 0$. Therefore, all terms in (6) evaluated at $x = x_w$ vanish. The arbitrariness of the variations $\delta\phi$, δh and $\delta\check{\phi}$ in the resulting variational principle yields the governing equations for the fluid domain. Specifically, in the deep-water subdomain, nonlinear potential-flow equations arises as follows:

$$
\delta\phi: \quad \partial_{xx}\phi + \partial_{zz}\phi = 0, \qquad \text{in } \Omega_D, \tag{7a}
$$

$$\delta h: \quad \partial_t\phi + \frac{1}{2}|\nabla\phi|^2 + g(h-H) = 0, \qquad \text{at } z = b+h, \tag{7b}$$

$$\delta\phi_{z=b+h}: \quad \partial_t h + \partial_x(b+h)\,\partial_x\phi - \partial_z\phi = 0, \qquad \text{at } z = b+h, \tag{7c}$$

$$\delta\phi_{z=b}: \quad \partial_x\phi\, b_x - \partial_z\phi = 0, \qquad \text{at } z = b, \tag{7d}$$

$$\delta\phi_{x=R}: \quad \partial_x\phi = \dot{R}, \qquad \text{at } x = R, \tag{7e}$$

whilst in the shallow-water domain, the depth-averaged nonlinear potential-flow equations takes the form:

$$\delta\check{\phi}: \quad \partial_t h + \partial_x h\,\partial_x\check{\phi} + h\,\partial_{xx}\check{\phi} = 0, \qquad \text{in } \Omega_S, \tag{8a}$$

$$\delta h: \quad \partial_t\check{\phi} + \frac{1}{2}(\partial_x\check{\phi})^2 + g(h-H) = 0, \qquad \text{in } \Omega_S, \tag{8b}$$

or, equivalently, the nonlinear shallow-water equations in conservative form, expressed in terms of h and $u \equiv \partial_x\check{\phi}$:

$$\partial_t h + \partial_x(hu) = 0, \qquad \text{in } \Omega_S, \tag{9a}$$

$$\partial_t(hu) + \partial_x\left(hu^2 + \frac{1}{2}gh^2\right) = -ghb_x, \qquad \text{in } \Omega_S. \tag{9b}$$

Deep- and shallow-water subdomains are connected at the interface $\Gamma_c = \{x = x_c, z \in [b, b+h]\}$, so the boundary terms arising from variations at $x = x_c$, i.e. the penultimate line in (6), must be analysed together to derive appropriate coupling conditions. This analysis is presented in the next section.

2.3 Coupling conditions at the interface

In this section, coupling conditions for both the deep- and shallow-water subdomains are derived from the two boundary terms evaluated at x_c in the variational principle (6).

On the one hand, given the depth-averaged relation (5), setting and substituting (as in [21])

$$\left(\delta\check{\phi}\right)_{x=x_c} = \left(\frac{1}{h}\int_b^{b+h} \delta\phi\,\mathrm{d}z\right)_{x=x_c} \tag{10}$$

leads to the coupling boundary condition for the deep-water equations:

$$h\partial_x\phi = h\partial_x\check{\phi} = hu \quad \text{for} \quad b \le z \le b+h \text{ at } x = x_c. \tag{11}$$

On the other hand, by setting and substituting

$$(\delta\phi)_{x=x_c} = \left(\delta\check{\phi}\right)_{x=x_c}, \tag{12}$$

we obtain the coupling boundary condition for the shallow-water equations:

$$h\partial_x\check{\phi} = \int_b^{b+h} \partial_x\phi \,\mathrm{d}z \qquad \text{at } x = x_c, \tag{13}$$

which, in terms of h and hu, reads

$$hu = \int_b^{b+h} \partial_x\phi \,\mathrm{d}z \qquad \text{at } x = x_c. \tag{14}$$

The rationale for these approximations is as follows: the variation $\delta\check{\phi}$ in the shallow-water limit $x \to x_c^+$ is readily seen to be the depth-averaged $\delta\phi$ in the deep-water limit $x \to x_c^-$, whilst the second condition implies that the coupling point x_c should be chosen such that shoaling into shallow water leads to nearly depth-independent flow, i.e. an approximately depth-uniform velocity profile.

Accordingly, the deep-water potential-flow equations (7) must be solved together with the nonlinear shallow-water equations (9), subject to the coupling conditions (11) and (14). NB These latter two conditions are in essence the same provided that the potential-flow dynamics have become close to depth-independent in the shallow waters of the surf zone. The point x_c of coupling between the two models is chosen based on the ratio between the typical wave length involved and the water depth, augmented with a posteriori inspection of the depth-profile of the velocity potential $\phi(x_c, z, t)$. The next section outlines the numerical strategy used to solve and couple these two systems.

3 Numerical coupling strategies of the coupled wavetank

In this section, we develop numerical strategies for discretising and coupling the nonlinear potential-flow and nonlinear shallow-water equations. The numerical coupling addresses several challenges, including handling time-dependent boundaries at the wavemaker $x = R(t)$, at the free surface $z = b(x) + h(x, t)$ and at the waterline $x = x_w(t)$; capturing breaking waves at the beach; and ensuring consistent and accurate information transfer across the interface Γ_c between the deep- and shallow-water domains. The spatial and temporal discretisation methods, along with their implementation in Firedrake, are now presented.

3.1 Spatial discretisation of the deep- and shallow-water subdomains

3.1.1 Discretisation of the deep-water subdomain

For the deep-water subdomain, the numerical model developed in [5–7], based on explicit weak formulations, is employed in its two-dimensional form. A σ-coordinate

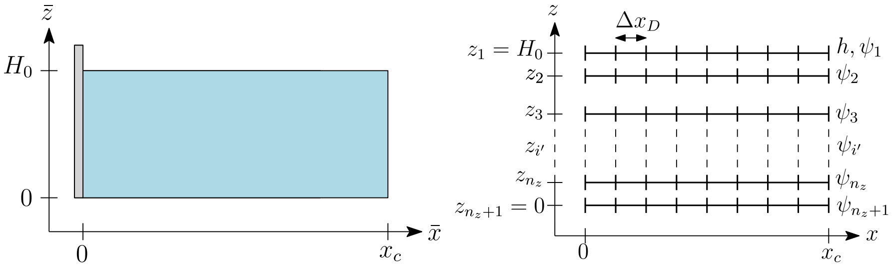

Fig. 2 Left: Fixed deep-water computational domain (blue), defined as Ω_D after applying the coordinate transformation. Right: Discretised deep-water domain, consisting of $n_z + 1$ vertical layers placed at Gauss–Lobatto–Legendre (GLL) points to mitigate the Runge effect, with each layer containing N_e horizontal elements of uniform width Δx_D

transformation [23] is applied prior to spatial discretisation:

$$x \quad \rightarrow \quad \bar{x} = \frac{x - \tilde{R}(x,t)}{L_w - \tilde{R}(x,t)} L_w \qquad \text{and} \qquad z \quad \rightarrow \quad \bar{z} = (z - b(x)) \frac{H_0}{h(x,t)}, \tag{15}$$

with $L_w = O(\lambda)$ and

$$\tilde{R}(x,t) = R(t)\Theta(L_w - x) = \begin{cases} R(t), & \text{if } x \leq L_w, \\ 0, & \text{if } x > L_w. \end{cases} \tag{16}$$

This transformation (15) maps the time-dependent physical deep-water subdomain (1) onto a fixed rectangular computational domain

$$\bar{\Omega}_D = \{0 \leq \bar{x} \leq x_c; 0 \leq \bar{z} \leq H_0\}, \tag{17}$$

as illustrated in Fig. 2. This approach circumvents the need for mesh regeneration at each time step due to the *a priori* unknown $h(x,t)$.

The resulting variational principle in transformed coordinates for the deep-water subdomain reads

$$\begin{aligned} 0 = \delta \int_0^T \Bigg\{ & \int_0^{x_c} \int_0^{H_0} \left[\frac{1}{2\Upsilon} h \Big(\phi_x - \frac{1}{h} \big(H_0 \underline{\underline{b_x}} + z h_x \big) \phi_z \Big)^2 + \frac{\Upsilon}{2} \frac{1}{h} (\phi_z)^2 \right] \mathrm{d}z \, \mathrm{d}x \\ & + \int_0^{x_c} \frac{1}{L_w} \Big[g W h \Big(\frac{1}{2} h - H \Big) - \phi \big(W h_t + X \tilde{R}_t \, h_x \big) \Big]_{z = H_0} \mathrm{d}x \\ & + \int_0^{H_0} \Big(\frac{1}{H_0} \tilde{R}_t \, \phi \, h \Big)_{x=0} \mathrm{d}z \Bigg\} \mathrm{d}t, \end{aligned} \tag{18a}$$

where, for clarity, the over-bars have been and will henceforth be omitted, and

$$X(x) = x - L_w, \quad W(x,t) = L_w - \tilde{R}(x,t), \quad \Upsilon(x,t) = \frac{W H_0}{L_w}. \tag{18b}$$

Note that the double-underlined topography gradient b_x in the kinetic energy expression in (18a) was accidentally ignored in earlier work [5, 24] due to the application of the mild-slope approximation (MSA). We will later show and compare simulations of the complete potential-flow equations (denoted by FWF) as well as ones with the MSA. The MSA is commonly used in Boussinesq-type approximations, in which the vertical integration is performed explicitly. It then yields an equation set with only horizontal spatial coordinates and the MSA then simplifies the expressions, e.g. see [25]. That MSA reduction is only minor in the full potential-flow setting used here.

As shown in Fig. 2, the deep-water computational domain is divided into N_e rectangular elements of size $\Delta x_D \times H_0$. In the vertical direction, the velocity potential $\phi(x, z, t)$ is expanded along the depth of each element using Lagrange polynomials $\tilde{\varphi}_i(z)$ of order n_z (cf. [5, 6]), such that

$$\begin{aligned} \phi(x, z, t) &= \psi_i(x, t)\tilde{\varphi}_i(z) = \psi_1(x, t)\tilde{\varphi}_1(z) + \psi_{i'}(x, t)\tilde{\varphi}_{i'}(z) \\ &= \begin{cases} \psi_1(x, t) \equiv \phi(x, H_0, t) & \text{at } z = H_0 \\ \psi_{i'}(x, t) \equiv \phi(x, z_{i'}, t) & \text{at } z = z_{i'} < H_0 \end{cases}, \end{aligned} \tag{19}$$

where the discrete vertical nodes $z_i \in [0, H_0]$ correspond to the scaled Gauss–Lobatto–Legendre (GLL) quadrature points. Note that the Einstein summation convention is used; and, ψ_1 as well as $\psi_{i'}$ are not streamfunctions. The subscripts $i \in [1, n_z + 1]$ and $i' \in [2, n_z + 1]$ distinguish the free-surface velocity potential ψ_1 from the interior values $\psi_{i'}$.

By substituting the expansion (19) into the transformed variational principle, the original two-dimensional formulation is reduced to a one-dimensional form:

$$\begin{aligned} 0 =& \delta \int_0^T \Bigg\{ \int_0^{x_c} \Bigg[\frac{1}{2\Upsilon} \Bigg(h\, \psi_{i,x} \tilde{M}_{ij} \psi_{j,x} - 2h_x \psi_{i,x} \tilde{D}_{ij} \psi_j - 2H_0 b_x \psi_{i,x} \tilde{B}_{ij} \psi_j \\ &+ 2H_0 \frac{b_x h_x}{h} \psi_i \tilde{C}_{ij} \psi_j + \frac{h_x^2}{h} \psi_i \tilde{S}_{ij} \psi_j \Bigg) + \left(\frac{1}{\Upsilon} H_0^2 b_x^2 + \Upsilon \right) \left(\frac{1}{2h} \psi_i \tilde{A}_{ij} \psi_j \right) \\ &+ \frac{1}{H_0} \Upsilon g h \left(\frac{1}{2} h - H \right) - \psi_1 \left(\frac{1}{H_0} \Upsilon h_t + \frac{1}{L_w} X \tilde{R}_t\, h_x \right) \Bigg] \mathrm{d}x \\ &+ \left(\frac{1}{H_0} \tilde{R}_t \psi_i \tilde{I}_i h \right)_{x=0} \Bigg\} \mathrm{d}t, \end{aligned} \tag{20}$$

where $i, j \in [1, n_z + 1]$, and the matrices $\tilde{A}$, $\tilde{B}$, $\tilde{C}$, $\tilde{D}$, $\tilde{I}$, $\tilde{M}$, and $\tilde{S}$ are defined as

$$\begin{aligned} \tilde{M}_{ij} &= \int_0^{H_0} \tilde{\varphi}_i(z) \tilde{\varphi}_j(z)\, \mathrm{d}z, & \tilde{A}_{ij} &= \int_0^{H_0} \frac{\mathrm{d}\tilde{\varphi}_i(z)}{\mathrm{d}z} \frac{\mathrm{d}\tilde{\varphi}_j(z)}{\mathrm{d}z}\, \mathrm{d}z, \\ \tilde{B}_{ij} &= \int_0^{H_0} \tilde{\varphi}_i(z) \frac{\mathrm{d}\tilde{\varphi}_j(z)}{\mathrm{d}z}\, \mathrm{d}z, & \tilde{C}_{ij} &= \int_0^{H_0} z \frac{\mathrm{d}\tilde{\varphi}_i(z)}{\mathrm{d}z} \frac{\mathrm{d}\tilde{\varphi}_j(z)}{\mathrm{d}z}\, \mathrm{d}z, \end{aligned}$$

$$
\begin{aligned}
&\tilde{D}_{ij} = \int_0^{H_0} z\tilde{\varphi}_i(z)\frac{\mathrm{d}\tilde{\varphi}_j(z)}{\mathrm{d}z}\,\mathrm{d}z, \qquad \tilde{S}_{ij} = \int_0^{H_0} z^2\frac{\mathrm{d}\tilde{\varphi}_i(z)}{\mathrm{d}z}\frac{\mathrm{d}\tilde{\varphi}_j(z)}{\mathrm{d}z}\,\mathrm{d}z,\\
&\tilde{I}_i = \int_0^{H_0}\tilde{\varphi}_i(z)\,\mathrm{d}z.
\end{aligned}
\tag{21}
$$

The transformed z-discretised nonlinear potential-flow equations can be derived from the variational principle (20). Taking variations with respect to h and applying integration by parts in space yields

$$
\begin{aligned}
0 = \int_0^T \Bigg\{ \int_0^{x_c} \delta h \bigg[&\frac{1}{2\Upsilon}\psi_{i,x}\tilde{M}_{ij}\psi_{j,x} + \frac{\partial}{\partial x}\Big(\frac{1}{\Upsilon}\psi_{i,x}\tilde{D}_{ij}\psi_j\Big)\\
&- \frac{\partial}{\partial x}\Big(\frac{1}{\Upsilon}\frac{h_x}{h}\psi_i\tilde{S}_{ij}\psi_j\Big) - \frac{1}{\Upsilon}\frac{(h_x)^2}{2h^2}\psi_i\tilde{S}_{ij}\psi_j - \frac{1}{2h^2}\left(\frac{H_0^2}{\Upsilon}b_x^2 + \Upsilon\right)\psi_i\tilde{A}_{ij}\psi_j\\
&- \frac{\partial}{\partial x}\Big(\frac{H_0}{\Upsilon}\frac{b_x}{h}\psi_i\tilde{C}_{ij}\psi_j\Big) - \frac{H_0 b_x}{\Upsilon}\frac{h_x}{h^2}\psi_i\tilde{C}_{ij}\psi_j\\
&+ \frac{\Upsilon}{H_0}g(h-H) + \frac{1}{L_w}\partial_t(W\psi_1) + \frac{\partial}{\partial x}\Big(\psi_1\frac{X}{L_w}\tilde{R}_t\Big)\bigg]\mathrm{d}x\\
&+ \Big\{\frac{1}{H_0}\tilde{R}_t\,\psi_i\tilde{I}_i\delta h\Big\}\Big|_{x=0} - \Big\{\frac{1}{\Upsilon}\delta h\,\psi_{i,x}\tilde{D}_{ij}\psi_j\Big\}\Big|_{x=0}^{x=x_c} + \Big\{\psi_1\frac{X}{L_w}\tilde{R}_t\delta h\Big\}\Big|_{x=0}\\
&+ \Big\{\frac{1}{\Upsilon}\frac{h_x\delta h}{h}\psi_i\tilde{S}_{ij}\psi_j\Big\}\Big|_{x=0}^{x=x_c} + \Big\{\frac{H_0 b_x}{\Upsilon}\frac{\delta h}{h}\psi_i\tilde{C}_{ij}\psi_j\Big\}\Big|_{x=0}^{x=x_c}\Bigg\}\,\mathrm{d}t,
\end{aligned}
\tag{22}
$$

from which the transformed dynamic boundary condition (7b) can be recovered as

$$
\begin{aligned}
&\frac{1}{L_w}\partial_t(W\psi_1)\\
&\quad= -\frac{1}{2\Upsilon}\psi_{i,x}\tilde{M}_{ij}\psi_{j,x} + \frac{1}{2\Upsilon}\frac{(h_x)^2}{h^2}\psi_i\tilde{S}_{ij}\psi_j + \frac{H_0}{\Upsilon}\frac{b_x h_x}{h^2}\psi_i\tilde{C}_{ij}\psi_j\\
&\quad+ \frac{\partial}{\partial x}\Big(-\frac{1}{\Upsilon}\psi_{i,x}\tilde{D}_{ij}\psi_j + \frac{1}{\Upsilon}\frac{h_x}{h}\psi_i\tilde{S}_{ij}\psi_j + \frac{H_0}{\Upsilon}\frac{b_x}{h}\psi_i\tilde{C}_{ij}\psi_j - \psi_1\frac{X}{L_w}\tilde{R}_t\Big)\\
&\quad+ \frac{1}{2h^2}\Big(\frac{H_0^2}{\Upsilon}b_x^2 + \Upsilon\Big)\psi_i\tilde{A}_{ij}\psi_j - \frac{\Upsilon}{H_0}g(h-H).
\end{aligned}
\tag{23}
$$

Similarly, taking variations with respect to ψ_j with $j \in [1, n_z+1]$ and applying integration by parts in space yields

$$
\begin{aligned}
0 = \int_0^T \Bigg\{ \int_0^{x_c} \delta\psi_j \bigg[&\frac{\partial}{\partial x}\Big(-\frac{1}{\Upsilon}h\,\psi_{i,x}\tilde{M}_{ij}\Big) + \frac{1}{\Upsilon}\frac{h_x^2}{h}\psi_i\tilde{S}_{ij}\\
&+ \frac{1}{h}\Big(\frac{H_0^2}{\Upsilon}b_x^2 + \Upsilon\Big)\psi_i\tilde{A}_{ij} + \frac{H_0}{\Upsilon}\frac{2b_x h_x}{h}\psi_i\tilde{C}_{ij}\\
&+ \frac{\partial}{\partial x}\Big(\frac{H_0}{\Upsilon}b_x\tilde{B}_{ji}\psi_i\Big) - \frac{H_0}{\Upsilon}b_x\psi_{i,x}\tilde{B}_{ij}
\end{aligned}
$$

$$
\begin{aligned}
&+\frac{\partial}{\partial x}\Big(\frac{1}{\Upsilon}h_x\tilde{D}_{ji}\psi_i\Big)-\frac{1}{\Upsilon}h_x\psi_{i,x}\tilde{D}_{ij}-\delta_{1j}\Big(\frac{\Upsilon}{H_0}h_t+\frac{X}{L_w}\tilde{R}_t\,h_x\Big)\Big]\mathrm{d}x\\
&+\Big\{\frac{1}{H_0}\tilde{R}_t\delta\psi_j\tilde{I}_j h\Big\}\Big|_{x=0}+\Big\{\frac{1}{\Upsilon}h\,\psi_{i,x}\tilde{M}_{ij}\delta\psi_j\Big\}\Big|_{x=0}^{x=x_c}\\
&-\Big\{\frac{H_0}{\Upsilon}b_x\delta\psi_j\tilde{B}_{ji}\psi_i\Big\}\Big|_{x=0}^{x=x_c}-\Big\{\frac{1}{\Upsilon}h_x\delta\psi_j\tilde{D}_{ji}\psi_i\Big\}\Big|_{x=0}^{x=x_c}\Big\}\,\mathrm{d}t,
\end{aligned}
\tag{24}
$$

from which the transformed potential-flow equation emerges as

$$
\begin{aligned}
\delta_{1j}\frac{\Upsilon}{H_0}h_t=&\frac{\partial}{\partial x}\Big(-\frac{1}{\Upsilon}h\,\psi_{i,x}\tilde{M}_{ij}+\frac{H_0}{\Upsilon}b_x\tilde{B}_{ji}\psi_i+\frac{1}{\Upsilon}h_x\tilde{D}_{ji}\psi_i\Big)\\
&+\frac{1}{h}\Big(\frac{H_0^2}{\Upsilon}b_x^2+\Upsilon\Big)\psi_i\tilde{A}_{ij}+\frac{H_0}{\Upsilon}\frac{2b_xh_x}{h}\psi_i\tilde{C}_{ij}+\frac{1}{\Upsilon}\frac{h_x^2}{h}\psi_i\tilde{S}_{ij}\\
&-\frac{H_0}{\Upsilon}b_x\psi_{i,x}\tilde{B}_{ij}-\frac{1}{\Upsilon}h_x\psi_{i,x}\tilde{D}_{ij}-\delta_{1j}\frac{X}{L_w}\tilde{R}_t\,h_x,
\end{aligned}
\tag{25}
$$

where δ_{1j} is the Kronecker delta. Note that in (25), the case $j=1$ corresponds to the transformed kinematic boundary condition (7c), whereas for $j=j'\in[2,n_z+1]$, it corresponds to the transformed Laplace's equation (7a). The transformed potential-flow equations (23) and (25) will be used in the derivation of the coupling condition for the shallow-water subdomain in Section 3.2.

Finally, in the horizontal direction, the unknowns $\psi_1(x,t)$, $\psi_{i'}(x,t)$, and $h(x,t)$ are expanded using first-order continuous Galerkin basis function as follows:

$$
\psi_1(x,t)=\psi_{1q}(t)\varphi_q(x),\quad \psi_{i'}(x,t)=\psi_{i'q}(t)\varphi_q(x),\quad h(x,t)=h_q(t)\varphi_q(x),
\tag{26a}
$$

where $\varphi_q(x)$ are the piecewise linear basis functions defined over the horizontal extent of the deep-water domain, $x\in[0,x_c]$. The horizontal node index q runs from $q=0$ at the wavemaker boundary $x=0$ to $q=N_e$ at the coupling point $x=x_c$. In the right-most element $[x_c-\Delta x_D, x_c]$, adjacent to the coupling point, the superscript $^-$ is used to indicate that only the left-hand side of the coupling point $x=x_c$ is included in the deep-water discretisation; that is, the basis function $\varphi_{N_e}^-$, with shorter notation φ_{c^-}, is nonzero only within this final element.

3.1.2 Discretisation of the shallow-water subdomain

Energy dissipation through bore formation and wave breaking is expected to be modelled in the shallow-water subdomain. The finite-element approach adopted in the deep-water subdomain, which is based on continuous expansions, would not remain stable due to the steep gradients associated with breaking waves. Instead, a Godunov-type finite-volume method is implemented to accommodate such breaking waves [19].

In the physical shallow-water domain Ω_S defined by (2), the coupling location at $x=x_c$ is fixed, whereas the waterline at $x=x_w$ moves along the sloping beach. To

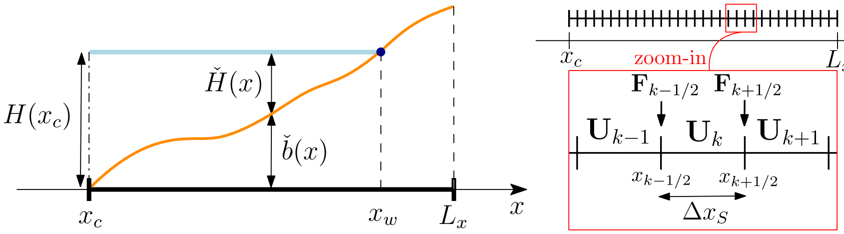

Fig. 3 Left: Fixed shallow-water computational domain (bold line segment) as defined by $\bar{\Omega}_S = [x_c, L_x]$. The local rest depth $\check{H}(x)$ and beach topography $\check{b}(x)$ are also illustrated. Right: Discretised shallow-water domain consists of N_v volumes of uniform size Δx_S

avoid mesh deformation caused by the moving boundary $x_w(t)$, a fixed right boundary is imposed at $x = L_x > \max_t\{x_w(t)\}$ such that the equations are solved over a time-independent one-dimensional numerical domain

$$\bar{\Omega}_S = \{x_c \leq x \leq L_x\}, \tag{27}$$

as illustrated by the bold line segment in Fig. 3. In the computational model, local variables are defined over the shallow-water domain $\bar{\Omega}_S$. The local beach topography is given by

$$\check{b}(x) = b(x) - b(x_c), \tag{28}$$

such that $\check{b}(x_c) = 0$, whilst the local rest depth is taken to be $\check{H}(x) = H(x)$. They are related through $\check{H}(x) = H(x_c) - \check{b}(x)$, see also Fig. 3.

To apply the finite-volume discretisation, the conservative form of the nonlinear shallow-water equations (9) is used and rewritten as

$$\partial_t \mathbf{U} + \partial_x \mathbf{F}(\mathbf{U}) = \mathbf{S}, \tag{29a}$$

where the state vector $\mathbf{U}$, the flux vector $\mathbf{F}(\mathbf{U})$ and the source term $\mathbf{S}$ are defined as

$$\mathbf{U} = \begin{pmatrix} h \\ hu \end{pmatrix}, \quad \mathbf{F}(\mathbf{U}) = \begin{pmatrix} hu \\ hu^2 + \frac{1}{2}gh^2 \end{pmatrix}, \quad \text{and} \quad \mathbf{S} = \begin{pmatrix} 0 \\ -gh\check{b}_x \end{pmatrix}. \tag{29b}$$

As shown in Fig. 3, the domain $\bar{\Omega}_S$ is discretised into N_v control volumes of uniform size Δx_S. In the kth volume, defined by $[x_{k-1/2}, x_{k+1/2}]$, the solution $\mathbf{U}$ is approximated by its cell average:

$$\mathbf{U}_k(t) = \frac{1}{\Delta x_S} \int_{x_{k-1/2}}^{x_{k+1/2}} \mathbf{U}(x, t)\, \mathrm{d}x, \tag{30}$$

which may be viewed as a zeroth-order discontinuous Galerkin approximation. Similarly, the local beach topography $\check{b}(x)$ is also approximated by its cell average:

$$\check{b}_k = \frac{1}{\Delta x_S} \int_{x_{k-1/2}}^{x_{k+1/2}} \check{b}(x)\, \mathrm{d}x. \tag{31}$$

The basis functions associated with $\mathbf{U}_k$ are discontinuous and taken to be piecewise constant within each control volume (i.e. C^0 continuous). In contrast, the deep-water variables are represented using piecewise linear basis functions that are C^1 continuous across nodes. To achieve a comparable order of accuracy between the shallow- and deep-water subdomains, the spatial resolutions are related by

$$\Delta x_S \propto (\Delta x_D)^2\,, \tag{32}$$

which ensures consistent matching between the leading-order finite-volume method and the first-order finite-element method.

Integration of the conservative form (29) over cell k yields the space-discretised nonlinear shallow-water equations:

$$\dot{\mathbf{U}}_k(t) + \frac{1}{\Delta x_S}\left(\mathbf{F}_{k+1/2}(t) - \mathbf{F}_{k-1/2}(t)\right) = \frac{1}{\Delta x_S}\mathbf{S}_k, \tag{33}$$

where the dot denotes a time derivative. The discrete flux

$$\mathbf{F}_{k\pm1/2}(t) = \mathbf{F}(\mathbf{U}(x_{k\pm1/2}, t)), \tag{34}$$

is evaluated at the cell interfaces $x = x_{k\pm1/2}$ using the Harten–Lax–van Leer (HLL) flux [26, 27]. The discretised source term $\mathbf{S}_k$ is evaluated using a hydrostatic reconstruction described shortly. Figure 3 also the locations where fluxes and state variables are evaluated.

To solve the system (29), the well-balanced finite-volume scheme developed by Audusse et al. [20] is employed with its ability to handle the wet–dry interface that arises due to the moving shoreline on a sloping beach. The scheme is designed to preserve conservation of total water mass and non-negativity of h in the dry region ($x_w(t) \leq x \leq L_x$), thereby ensuring numerical stability, for reference see Appendix B.

3.2 Discretised coupling conditions at the interface

Following the finite-volume discretisation, the cell-averaged shallow-water velocity u_k satisfies

$$\begin{aligned} u_k =& \frac{1}{\Delta x_S}\int_{x_{k-1/2}}^{x_{k+1/2}} u(x,t)\,\mathrm{d}x = \frac{1}{\Delta x_S}\int_{x_{k-1/2}}^{x_{k+1/2}} \partial_x\check{\phi}(x,t)\,\mathrm{d}x \\ =& \frac{1}{\Delta x_S}\left[\check{\phi}(x_{k+1/2},t) - \check{\phi}(x_{k-1/2},t)\right]. \end{aligned} \tag{35}$$

This discrete piecewise constant shallow-water velocity can thus be expressed in terms of the shallow-water velocity potential $\check{\phi}(x,t)$, approximated at the cell interfaces via

$$\check{\phi}(x,t) = \check{\phi}_l(t)\varphi_l(x), \tag{36}$$

where $\varphi_l(x)$ is the first-order piecewise linear basis function defined in $\bar{\Omega}_S$ (cf. (26)), and the index l runs from $l = N_e$ at $x = x_c$ to $l = N_e + N_v$ at $x = L_x$. It should be noted that only the right-hand side of the coupling location $x = x_c$ is included in the shallow-water discretisation. Therefore, the basis function φ_{c^+}, short hand for $\varphi^+_{N_e}$, is nonzero only within the first cell to the right of the interface, i.e. $[x_c, x_c + \Delta x_S]$.

Replacing the deep-water variational principle in (4) with its transformed z-discretised version (20), we obtain the variational principle for the entire domain:

$$\begin{aligned}
0 =&\delta \int_0^T \Bigg\{ \int_0^{x_c} \Bigg[\frac{1}{2\Upsilon} \Big(h\,\psi_{i,x} \tilde{M}_{ij} \psi_{j,x} - 2h_x \psi_{i,x} \tilde{D}_{ij} \psi_j - 2H_0 b_x \psi_{i,x} \tilde{B}_{ij} \psi_j \\
&+ 2H_0 \frac{b_x h_x}{h} \psi_i \tilde{C}_{ij} \psi_j + \frac{h_x^2}{h} \psi_i \tilde{S}_{ij} \psi_j \Big) + \Big(\frac{1}{\Upsilon} H_0^2 b_x^2 + \Upsilon \Big) \Big(\frac{1}{2h} \psi_i \tilde{A}_{ij} \psi_j \Big) \\
&+ \frac{1}{H_0} \Upsilon g h \Big(\frac{1}{2} h - H \Big) - \psi_1 \Big(\frac{1}{H_0} \Upsilon h_t + \frac{1}{L_w} X \tilde{R}_t\, h_x \Big) \Bigg] \mathrm{d}x + \Big(\frac{1}{H_0} \tilde{R}_t \psi_i \tilde{I}_i h \Big)_{x=0} \\
&+ \int_{x_c}^{L_x} \Big[h \partial_t \check{\phi} + \frac{1}{2} h (\partial_x \check{\phi})^2 + gh \Big(\frac{1}{2} h - H \Big) \Big] \mathrm{d}x \Bigg\} \mathrm{d}t. \qquad (37)
\end{aligned}$$

The space-discretised coupling conditions for both the deep- and shallow-water subdomains, which arise from the variational equations associated with φ_{c^+} and φ_{c^-}, respectively, are now derived from (37). Briefly, the remainder of this section consists of a technical and intricate derivation of the numerical coupling. In essence, the derivation consists of systematically accounting for the exchange terms arising from the variations in (37) by relating these φ_{c^+} and φ_{c^-} variations using discretisations of the continuum coupling conditions (11) and (14).

3.2.1 Coupling conditions for the deep-water subdomain

At the coupling node $x = x_c$, the shallow-water potential $\check{\phi}_c \equiv \check{\phi}(x = x_c, t)$ corresponds to the depth-averaged deep-water velocity potential (cf. (5)), and it can be computed as follows:

$$\begin{aligned}
\check{\phi}_c &= \frac{1}{h} \int_b^{b+h} \phi(x = x_c, z, t)\, \mathrm{d}z = \frac{1}{h} \int_0^{H_0} \bar{\phi}(\bar{x} = x_c, \bar{z}, \bar{t}) \frac{h}{H_0}\, \mathrm{d}\bar{z} \\
&= \frac{1}{H_0} \psi_i(\bar{x} = x_c, \bar{t}) \int_0^{H_0} \tilde{\varphi}_i(\bar{z})\, \mathrm{d}\bar{z} = \frac{1}{H_0} \psi_{ic} \tilde{I}_i.
\end{aligned} \qquad (38)$$

Since $\check{\phi}_c$ is evaluated at the interface Γ_c, its variation $\delta\check{\phi}_c$ should also follow the coordinate transformation (15), which transforms the variation of the deep-water velocity potential into

$$\delta\phi \to -\frac{\bar{z}}{h} \partial_{\bar{z}} \bar{\phi}\, \delta h + \delta\bar{\phi}. \qquad (39)$$

As a result, the variation of $\check{\phi}_c$ evaluated at $x = x_c^+$ becomes

$$\begin{aligned}\delta\check{\phi}_c &= \frac{1}{h}\int_b^{b+h} \delta\phi(x = x_c, z, t)\,\mathrm{d}z \\ &= \frac{1}{h}\int_0^{H_0} \left(\delta\bar{\phi}(\bar{x} = x_c, \bar{z}, \bar{t}) - \frac{\bar{z}}{h}\partial_{\bar{z}}\bar{\phi}(\bar{x} = x_c, \bar{z}, \bar{t})\,\delta h\right)\frac{h}{H_0}\,\mathrm{d}\bar{z} \\ &= \frac{1}{H_0}\left(\delta\psi_i(x_c, t)\int_0^{H_0}\tilde{\varphi}_i(\bar{z})\,\mathrm{d}\bar{z} - \frac{\delta h(x_c, t)}{h(x_c, t)}\psi_i(x_c, t)\int_0^{H_0}\bar{z}\frac{\mathrm{d}\tilde{\varphi}_i}{\mathrm{d}\bar{z}}\,\mathrm{d}\bar{z}\right) \\ &= \frac{1}{H_0}\left(\delta\psi_{ic}\tilde{I}_i - \frac{\delta h_c}{h_c}\psi_{ic}\tilde{G}_i\right),\end{aligned} \tag{40}$$

with $\tilde{G}_i$ defined as

$$\tilde{G}_i = \int_0^{H_0} z\frac{\mathrm{d}\tilde{\varphi}_i}{\mathrm{d}z}\,\mathrm{d}z. \tag{41}$$

To derive the deep-water coupling conditions, we use the complete deep-water expansions (26), whilst the shallow-water expansion (36) is partitioned to distinguish the coupling node from the remaining shallow-water nodes as follows:

$$\begin{aligned}\check{\phi}(x, t) = \check{\phi}_l(t)\varphi_l(x) &= \check{\phi}_c(t)\varphi_{c^+}(x) + \check{\phi}_{l'}(t)\varphi_{l'}(x) \\ &= \frac{1}{H_0}\psi_{ic}(t)\tilde{I}_i\,\varphi_{c^+}(x) + \check{\phi}_{l'}(t)\varphi_{l'}(x)\end{aligned} \tag{42}$$

with the shallow-water indices $l \in [N_e, N_e + N_v]$ and $l' \in [N_e + 1, N_e + N_v]$. Substituting (40), the variation of $\check{\phi}$ becomes

$$\delta\check{\phi} = \frac{1}{H_0}\left(\delta\psi_{ic}\tilde{I}_i - \frac{\delta h_c}{h_c}\psi_{ic}\tilde{G}_i\right)\varphi_{c^+} + \delta\check{\phi}_{l'}\varphi_{l'}. \tag{43}$$

Taking variations with respect to deep-water variables ψ_{iq} and h_q, and the shallow-water variables $\check{\phi}_l$ and h in the variational principle (37), we obtain

$$\begin{aligned}0 = \int_0^T\int_0^{x_c} \delta\psi_{iq}\Bigg\{&\frac{1}{\Upsilon}\Bigg[h\frac{\mathrm{d}\varphi_q}{\mathrm{d}x}\partial_x\psi_j\tilde{M}_{ij} + \frac{1}{h}(\partial_x h)^2\psi_j\varphi_q\tilde{S}_{ij} \\ &- \partial_x h\left(\frac{\mathrm{d}\varphi_q}{\mathrm{d}x}\tilde{D}_{ij}\psi_j + \varphi_q\partial_x\psi_j\tilde{D}_{ji}\right) - H_0 b_x\left(\frac{\mathrm{d}\varphi_q}{\mathrm{d}x}\tilde{B}_{ij}\psi_j + \varphi_q\partial_x\psi_j\tilde{B}_{ji}\right)\Bigg] \\ &+ \frac{H_0}{\Upsilon}\frac{2b_x\partial_x h}{h}\varphi_q\psi_j\tilde{C}_{ij} + \frac{1}{h}\left(\frac{H_0^2}{\Upsilon}b_x^2 + \Upsilon\right)\varphi_q\psi_j\tilde{A}_{ij} \\ &+ \frac{\delta_{q0}}{H_0}\partial_t\tilde{R}\,h_0\tilde{I}_i - \Upsilon\frac{\delta_{i1}}{H_0}\varphi_q\left(\partial_t h + \frac{X}{W}\partial_t\tilde{R}\partial_x h\right)\Bigg\} \\ &+ \delta h_q\Bigg\{\frac{1}{2\Upsilon}\Bigg[\varphi_q\partial_x\psi_i\tilde{M}_{ij}\partial_x\psi_j + \left(-\frac{\varphi_q}{h^2}(\partial_x h)^2 + \frac{2}{h}\partial_x h\frac{\mathrm{d}\varphi_q}{\mathrm{d}x}\right)\psi_i\tilde{S}_{ij}\psi_j\end{aligned}$$

$$
\begin{aligned}
&- 2\frac{\mathrm{d}\varphi_q}{\mathrm{d}x}\partial_x\psi_i\tilde{D}_{ij}\psi_j\Bigg] + \frac{\Upsilon}{H_0}\left[\varphi_q g\,(h-H) - \psi_1\frac{X}{W}\partial_t\tilde{R}\frac{\mathrm{d}\varphi_q}{\mathrm{d}x}\right]\\
&- \frac{\varphi_q}{2h^2}\left(\frac{H_0^2}{\Upsilon}b_x^2 + \Upsilon\right)\psi_i\tilde{A}_{ij}\psi_j + \frac{H_0 b_x}{\Upsilon}\left(\frac{1}{h}\frac{\mathrm{d}\varphi_q}{\mathrm{d}x} - \frac{\varphi_q\partial_x h}{h^2}\right)\psi_i\tilde{C}_{ij}\psi_j\\
&+ \delta_{q0}\frac{1}{H_0}\partial_t\tilde{R}\;\psi_{i0}\tilde{I}_i + \frac{\varphi_q}{L_w}\partial_t(W\psi_1)\Bigg\}\,\mathrm{d}x\\
&+ \int_{x_c}^{L_x}\left\{\frac{1}{H_0}\Big(\delta\psi_{ic}\tilde{I}_i - \frac{\delta h_c}{h_c}\psi_{ic}\tilde{G}_i\Big)\left[-\partial_t h\,\varphi_{c^+} + h\partial_x\check{\phi}\,\frac{\mathrm{d}\varphi_{c^+}}{\mathrm{d}x}\right]\right.\\
&\left.+ \delta\check{\phi}_{l'}\left[-\partial_t h\,\varphi_{l'} + h\partial_x\check{\phi}\,\frac{\mathrm{d}\varphi_{l'}}{\mathrm{d}x}\right] + \delta h\left[\partial_t\check{\phi} + \frac{1}{2}\left(\partial_x\check{\phi}\right)^2 + g(h-H)\right]\right\}\mathrm{d}x\,\mathrm{d}t.
\end{aligned}
\tag{44}
$$

Substituting the shallow-water equations (8) into (44), the last two lines vanish. The remaining term in the integral over the shallow-water domain can be simplified by referring to the definition of φ_{c^+} and equation (8a) as follows:

$$
\begin{aligned}
&\int_0^T\int_{x_c}^{L_x}\frac{1}{H_0}\Big(\delta\psi_{ic}\tilde{I}_i - \frac{\delta h_c}{h_c}\psi_{ic}\tilde{G}_i\Big)\left[-\partial_t h\,\varphi_{c^+} + h\partial_x\check{\phi}\frac{\mathrm{d}\varphi_{c^+}}{\mathrm{d}x}\right]\mathrm{d}x\,\mathrm{d}t\\
&= \int_0^T\int_{x_c}^{x_c+\Delta x_S}\frac{1}{H_0}\Big(\delta\psi_{ic}\tilde{I}_i - \frac{\delta h_c}{h_c}\psi_{ic}\tilde{G}_i\Big)\left[\partial_x(h\partial_x\check{\phi})\,\varphi_{c^+} + h\partial_x\check{\phi}\frac{\mathrm{d}\varphi_{c^+}}{\mathrm{d}x}\right]\mathrm{d}x\,\mathrm{d}t\\
&= \int_0^T\frac{1}{H_0}\Big(\delta\psi_{ic}\tilde{I}_i - \frac{\delta h_c}{h_c}\psi_{ic}\tilde{G}_i\Big)\left\{h\partial_x\check{\phi}\,\varphi_{c^+}\right\}\Big|_{x_c}^{x_c+\Delta x_S}\mathrm{d}t\\
&= \int_0^T -\frac{1}{H_0}\Big(\delta\psi_{ic}\tilde{I}_i - \frac{\delta h_c}{h_c}\psi_{ic}\tilde{G}_i\Big)\left\{h\partial_x\check{\phi}\right\}\Big|_{x=x_c}\mathrm{d}t.
\end{aligned}
\tag{45}
$$

Substituting (45) into (44) yields the boundary terms at $x = x_c$ for the deep-water variations $\delta\psi_i$ and δh. The deep-water weak formulations with coupling boundary terms are thus given by the variation for $\delta\psi_j$

$$
\begin{aligned}
0 = &\int_0^{x_c}\Bigg[\frac{1}{\Upsilon}h\,\psi_{i,x}\tilde{M}_{ij}(\delta\psi_j)_x + \frac{1}{\Upsilon}\frac{h_x^2}{h}\psi_i\tilde{S}_{ij}\delta\psi_j\\
&+ \frac{1}{h}\Big(\frac{H_0^2}{\Upsilon}b_x^2 + \Upsilon\Big)\psi_i\tilde{A}_{ij}\delta\psi_j + \frac{H_0}{\Upsilon}\frac{2b_x h_x}{h}\psi_i\tilde{C}_{ij}\delta\psi_j\\
&- \frac{H_0}{\Upsilon}b_x\left((\delta\psi_j)_x\tilde{B}_{ji}\psi_i + \psi_{i,x}\tilde{B}_{ij}\delta\psi_j\right) - \frac{1}{\Upsilon}h_x\left((\delta\psi_j)_x\tilde{D}_{ji}\psi_i + \psi_{i,x}\tilde{D}_{ij}\delta\psi_j\right)\\
&- \delta_{1j}\left(\frac{W}{L_w}h_t + \frac{X}{L_w}\tilde{R}_t\,h_x\right)\delta\psi_j\Bigg]\mathrm{d}x + \frac{1}{H_0}\tilde{I}_j\left(\left\{R_t h\delta\psi_j\right\}\big|_{x=0} - \left\{hu\delta\psi_j\right\}\big|_{x=x_c}\right),
\end{aligned}
\tag{46}
$$

and the variation for δh

$$
\begin{aligned}
0 = \int_0^{x_c} \Bigg[& \frac{1}{2\Upsilon} \delta h\, \psi_{i,x} \tilde{M}_{ij} \psi_{j,x} + \frac{1}{\Upsilon} \left(\frac{h_x (\delta h)_x}{h} - \frac{\delta h (h_x)^2}{2h^2} \right) \psi_i \tilde{S}_{ij} \psi_j \\
& - \frac{\delta h}{2h^2} \left(\frac{H_0^2}{\Upsilon} b_x^2 + \Upsilon \right) \psi_i \tilde{A}_{ij} \psi_j + \frac{H_0 b_x}{\Upsilon} \left(\frac{(\delta h)_x}{h} - \frac{\delta h\, h_x}{h^2} \right) \psi_i \tilde{C}_{ij} \psi_j \\
& - \frac{1}{\Upsilon} (\delta h)_x\, \psi_{i,x} \tilde{D}_{ij} \psi_j + \frac{\Upsilon}{H_0} g \delta h (h - H) \\
& + \frac{1}{L_w} \delta h\, \partial_t (W \psi_1) - \psi_1 \frac{X}{L_w} \tilde{R}_t (\delta h)_x \Bigg] \mathrm{d}x \\
& + \frac{1}{H_0} \left(\left\{ \tilde{R}_t\, \psi_i \tilde{I}_i \delta h \right\} \Big|_{x=0} + \left\{ \frac{hu}{h} \psi_i \tilde{G}_i \delta h \right\} \Big|_{x=x_c} \right),
\end{aligned} \tag{47}
$$

where the shallow-water velocity $u \equiv \partial_x \check{\phi}$ has been substituted. The coupling terms are imposed weakly at the boundary $x = x_c$. Note that (46) represents a system of $n_z + 1$ equations, indexed by $j \in [1, n_z + 1]$. In particular, the case $j = 1$ governs the evolution of h, whilst the cases $j > 1$ determine the interior velocity potentials $\psi_{j'}$ in terms of the free-surface variables ψ_1 and h. The transformed z-discretised deep-water coupling conditions, corresponding to the continuous formulation in (11), are derived in Appendix A.

A.0.2 Coupling condition for the shallow-water subdomain

To derive the shallow-water coupling condition, the variations of the deep-water variables h and ψ_j need to be partitioned to isolate the coupling node from the remaining ones (cf. (26)) as follows:

$$
\delta h(x,t) = \delta h_q(t)\, \varphi_q(x) = \delta h_{q'}(t)\, \varphi_{q'}(x) + \delta h_c(t)\, \varphi_{c^-}(x), \tag{48a}
$$

$$
\delta \psi_j(x,t) = \delta \psi_{jq}(t)\, \varphi_q(x) = \delta \psi_{jq'}(t)\, \varphi_{q'}(x) + \delta \psi_{jc}(t)\, \varphi_{c^-}(x), \tag{48b}
$$

with the deep-water indices $q \in [0, N_e]$ and $q' \in [0, N_e - 1]$. Applying the partition (48a) to δh, the variation at the coupling node takes the form (cf. (44))

$$
\begin{aligned}
\int_0^T \Bigg\{ \delta h_c \int_0^{x_c} \Bigg[& \frac{1}{2\Upsilon} \varphi_{c^-}\, \psi_{i,x} \tilde{M}_{ij} \psi_{j,x} - \frac{1}{\Upsilon} \frac{\mathrm{d}\varphi_{c^-}}{\mathrm{d}x}\, \psi_{i,x} \tilde{D}_{ij} \psi_j \\
& + \frac{1}{\Upsilon} \left(\frac{h_x}{h} \frac{\mathrm{d}\varphi_{c^-}}{\mathrm{d}x} - \frac{\varphi_{c^-} (h_x)^2}{2h^2} \right) \psi_i \tilde{S}_{ij} \psi_j - \frac{\varphi_{c^-}}{2h^2} \left(\frac{H_0^2}{\Upsilon} b_x^2 + \Upsilon \right) \psi_i \tilde{A}_{ij} \psi_j \\
& + \frac{H_0 b_x}{\Upsilon} \left(\frac{1}{h} \frac{\mathrm{d}\varphi_{c^-}}{\mathrm{d}x} - \frac{\varphi_{c^-} h_x}{h^2} \right) \psi_i \tilde{C}_{ij} \psi_j \\
& + \frac{\Upsilon}{H_0} g \varphi_{c^-} (h - H) + \frac{\varphi_{c^-}}{L_w} \partial_t (W \psi_1) - \psi_1 \frac{X}{L_w} \tilde{R}_t \frac{\mathrm{d}\varphi_{c^-}}{\mathrm{d}x} \Bigg] \mathrm{d}x \Bigg\} \mathrm{d}t.
\end{aligned} \tag{49}
$$

Using the transformed potential-flow equation (23), expression (49) can be simplified as

$$\begin{aligned}
&\int_0^T \Bigg\{\delta h_c \Bigg[\int_0^{x_c} \frac{\mathrm{d}\varphi_{c^-}}{\mathrm{d}x}\Bigg[\frac{1}{\Upsilon}\left(\frac{h_x}{h}\psi_i \tilde{S}_{ij}\psi_j + \frac{H_0 b_x}{h}\psi_i \tilde{C}_{ij}\psi_j - \psi_{i,x}\tilde{D}_{ij}\psi_j\right) - \psi_1 \frac{X}{L_w}\tilde{R}_t\Bigg] \\
&\qquad + \varphi_{c^-}\frac{\partial}{\partial x}\Bigg[\frac{1}{\Upsilon}\left(\frac{h_x}{h}\psi_i \tilde{S}_{ij}\psi_j + \frac{H_0 b_x}{h}\psi_i \tilde{C}_{ij}\psi_j - \psi_{i,x}\tilde{D}_{ij}\psi_j\right) - \psi_1 \frac{X}{L_w}\tilde{R}_t\Bigg]\mathrm{d}x\Bigg]\Bigg\}\,\mathrm{d}t \\
&= \int_0^T \delta h_c \left\{\varphi_{c^-}\Bigg[\frac{1}{\Upsilon}\left(\frac{h_x}{h}\psi_i \tilde{S}_{ij}\psi_j + \frac{H_0 b_x}{h}\psi_i \tilde{C}_{ij}\psi_j - \psi_{i,x}\tilde{D}_{ij}\psi_j\right) - \psi_1 \frac{X}{L_w}\tilde{R}_t\Bigg]\right\}\Bigg|_{x=0}^{x=x_c}\mathrm{d}t \\
&= \int_0^T \delta h_c \frac{1}{H_0}\left\{\frac{h_x}{h}\psi_i \tilde{S}_{ij}\psi_j + \frac{H_0 b_x}{h}\psi_i \tilde{C}_{ij}\psi_j - \psi_{i,x}\tilde{D}_{ij}\psi_j\right\}\Bigg|_{x=x_c}\mathrm{d}t.
\end{aligned}$$

Applying partition (48b) to $\delta\psi_j$, the variation at the coupling node reads (cf. (44))

$$\begin{aligned}
&\int_0^T \Bigg\{\delta\psi_{jc}\int_0^{x_c}\Bigg[\frac{1}{\Upsilon}h\,\psi_{i,x}\tilde{M}_{ij}\frac{\mathrm{d}\varphi_{c^-}}{\mathrm{d}x} + \frac{1}{\Upsilon}\frac{h_x^2}{h}\psi_i \tilde{S}_{ij}\varphi_{c^-} \\
&\quad + \frac{1}{h}\left(\frac{H_0^2}{\Upsilon}b_x^2 + \Upsilon\right)\psi_i \tilde{A}_{ij}\varphi_{c^-} + \frac{H_0}{\Upsilon}\frac{2b_x h_x}{h}\psi_i \tilde{C}_{ij}\varphi_{c^-} \\
&\quad - \frac{H_0}{\Upsilon}b_x\left(\frac{\mathrm{d}\varphi_{c^-}}{\mathrm{d}x}\tilde{B}_{ji}\psi_i + \psi_{i,x}\tilde{B}_{ij}\varphi_{c^-}\right) \\
&\quad - \frac{1}{\Upsilon}h_x\left(\frac{\mathrm{d}\varphi_{c^-}}{\mathrm{d}x}\tilde{D}_{ji}\psi_i + \psi_{i,x}\tilde{D}_{ij}\varphi_{c^-}\right) - \delta_{1j}\left(\frac{\Upsilon}{H_0}h_t + \frac{X}{L_w}\tilde{R}_t\,h_x\right)\varphi_{c^-}\Bigg]\mathrm{d}x\Bigg\}\,\mathrm{d}t.
\end{aligned} \tag{50}$$

Using transformed potential-flow equation (25), expression (50) is simplified to

$$\begin{aligned}
&\int_0^T \Bigg\{\delta\psi_{jc}\Bigg[\int_0^{x_c}\frac{\mathrm{d}\varphi_{c^-}}{\mathrm{d}x}\Bigg[\frac{1}{\Upsilon}\left(h\,\psi_{i,x}\tilde{M}_{ij} - H_0 b_x \tilde{B}_{ji}\psi_i - h_x \tilde{D}_{ji}\psi_i\right)\Bigg] \\
&\qquad + \varphi_{c^-}\frac{\partial}{\partial x}\Bigg[\frac{1}{\Upsilon}\left(h\,\psi_{i,x}\tilde{M}_{ij} - h_x \tilde{D}_{ji}\psi_i - H_0 b_x \tilde{B}_{ji}\psi_i\right)\Bigg]\mathrm{d}x\Bigg]\Bigg\}\,\mathrm{d}t \\
&= \int_0^T \delta\psi_{jc}\left\{\varphi_{c^-}\frac{1}{\Upsilon}\left(h\,\psi_{i,x}\tilde{M}_{ij} - h_x \tilde{D}_{ji}\psi_i - H_0 b_x \tilde{B}_{ji}\psi_i\right)\right\}\Bigg|_{x=0}^{x=x_c}\mathrm{d}t \\
&= \int_0^T \delta\psi_{jc}\frac{1}{H_0}\left\{h\,\psi_{i,x}\tilde{M}_{ij} - h_x \tilde{D}_{ji}\psi_i - H_0 b_x \tilde{B}_{ji}\psi_i\right\}\Big|_{x=x_c}\mathrm{d}t.
\end{aligned}$$

Collecting results from the deep-water variations containing φ_{c^-}, i.e. simplified forms of (49) and (50), matters combine to

$$\begin{aligned}
&\int_0^T \frac{\delta\psi_{ic}}{H_0}\left\{h\,\psi_{j,x}\tilde{M}_{ij} - h_x \tilde{D}_{ij}\psi_j - H_0 b_x \tilde{B}_{ij}\psi_j\right\}\Big|_{x=x_c} \\
&\quad + \frac{\delta h_c}{H_0}\left\{\frac{h_x}{h}\psi_i \tilde{S}_{ij}\psi_j + \frac{H_0 b_x}{h}\psi_i \tilde{C}_{ij}\psi_j - \psi_{i,x}\tilde{D}_{ij}\psi_j\right\}\Bigg|_{x=x_c}\mathrm{d}t \\
&= \int_0^T \frac{\delta\psi_{ic}}{H_0}\left\{\int_0^{H_0}\tilde{\varphi}_i\left(h\psi_{j,x}\tilde{\varphi}_j - h_x\psi_j z\frac{\mathrm{d}\tilde{\varphi}_j}{\mathrm{d}z} - H_0 b_x \psi_j \frac{\mathrm{d}\tilde{\varphi}_j}{\mathrm{d}z}\right)\mathrm{d}z\right\}\Bigg|_{x=x_c}
\end{aligned}$$

$$\begin{aligned}
&- \frac{\delta h_c}{H_0} \left\{ \int_0^{H_0} z\psi_i \frac{\mathrm{d}\tilde{\varphi}_i}{\mathrm{d}z} \frac{1}{h} \left(-h_x \psi_j z \frac{\mathrm{d}\tilde{\varphi}_j}{\mathrm{d}z} - H_0 b_x \psi_j \frac{\mathrm{d}\tilde{\varphi}_j}{\mathrm{d}z} + h\psi_{j,x}\tilde{\varphi}_j \right) \mathrm{d}z \right\}\Bigg|_{x=x_c} \mathrm{d}t \\
= &\int_0^T \int_0^{H_0} \frac{\delta\psi_{ic}}{H_0}\tilde{\varphi}_i \left\{ h\psi_{j,x}\tilde{\varphi}_j - h_x\psi_j z \frac{\mathrm{d}\tilde{\varphi}_j}{\mathrm{d}z} - H_0 b_x \psi_j \frac{\mathrm{d}\tilde{\varphi}_j}{\mathrm{d}z} \right\}\Bigg|_{x=x_c} \mathrm{d}z \\
&- \int_0^{H_0} \frac{\delta h_c}{H_0} z\psi_{ic} \frac{\mathrm{d}\tilde{\varphi}_i}{\mathrm{d}z} \frac{1}{h_c} \left\{ -h_x\psi_j z \frac{\mathrm{d}\tilde{\varphi}_j}{\mathrm{d}z} - H_0 b_x \psi_j \frac{\mathrm{d}\tilde{\varphi}_j}{\mathrm{d}z} + h\psi_{j,x}\tilde{\varphi}_j \right\}\Bigg|_{x=x_c} \mathrm{d}z\, \mathrm{d}t \\
= &\int_0^T \int_0^{H_0} \frac{1}{H_0} \left(\delta\psi_{ic}\tilde{\varphi}_i - z\psi_{ic} \frac{\mathrm{d}\tilde{\varphi}_i}{\mathrm{d}z} \frac{\delta h_c}{h_c} \right) \left\{ h\psi_{j,x}\tilde{\varphi}_j - h_x\psi_j z \frac{\mathrm{d}\tilde{\varphi}_j}{\mathrm{d}z} - H_0 b_x \psi_j \frac{\mathrm{d}\tilde{\varphi}_j}{\mathrm{d}z} \right\}\Bigg|_{x=x_c} \mathrm{d}z\, \mathrm{d}t \\
= &\int_0^T \int_0^{H_0} \frac{1}{H_0} \delta\phi_c \left\{ h\psi_{j,x}\tilde{\varphi}_j - h_x\psi_j z \frac{\mathrm{d}\tilde{\varphi}_j}{\mathrm{d}z} - H_0 b_x \psi_j \frac{\mathrm{d}\tilde{\varphi}_j}{\mathrm{d}z} \right\}\Bigg|_{x=x_c} \mathrm{d}z\, \mathrm{d}t,
\end{aligned}$$

wherein relation (12) transformed by (15) is used:

$$\delta\psi_{ic}\tilde{\varphi}_i - \frac{\delta h_c}{h_c} z\, \psi_{ic} \frac{\mathrm{d}\tilde{\varphi}_i}{\mathrm{d}z} = \delta\phi_c. \tag{51}$$

In terms of the shallow-water variations, after performing integration by parts in space on the $\delta\check{\phi}_l$ equation (cf. (44)), i.e.

$$\int_0^T \int_{x_c}^{L_x} \delta\check{\phi}_l \left[-\partial_t h\, \varphi_l + h\partial_x\check{\phi}\, \frac{\mathrm{d}\varphi_l}{\mathrm{d}x} \right] \mathrm{d}x\, \mathrm{d}t, \tag{52}$$

a boundary term emerges at $x = x_c$, namely

$$\delta\check{\phi}|_{x=x_c} : \quad -h\partial_x\check{\phi}. \tag{53}$$

Collecting the boundary terms on both sides of $x = x_c$ leads to the coupling condition for the shallow-water region:

$$\begin{aligned}
\{hu\}|_{x=x_c} &= \frac{1}{H_0} \int_0^{H_0} \left\{ h\psi_{i,x}\tilde{\varphi}_i - h_x\psi_i z \frac{\mathrm{d}\tilde{\varphi}_i}{\mathrm{d}z} - H_0 b_x \psi_i \frac{\mathrm{d}\tilde{\varphi}_i}{\mathrm{d}z} \right\}\Bigg|_{x=x_c} \mathrm{d}z \\
&= \frac{1}{H_0} \left\{ h\psi_{i,x}\tilde{I}_i - h_x\psi_i\tilde{G}_i - H_0 b_x(\psi_1 - \psi_{n_z+1}) \right\}\Big|_{x=x_c}.
\end{aligned} \tag{54}$$

Alternatively, this coupling condition may also be obtained directly by transforming its continuous formulation (14), as shown in Appendix A. The boundary condition (54) is imposed on the shallow-water subdomain at $x = x_c$ via

$$\begin{pmatrix} h \\ hu \end{pmatrix}_{x=x_c} = \begin{pmatrix} h \\ \frac{1}{H_0}\left[h\partial_x\psi_i\tilde{I}_i - \psi_i\tilde{G}_i\partial_x h - H_0 b_x(\psi_1 - \psi_{n_z+1}) \right] \end{pmatrix}_{x=x_c}. \tag{55}$$

A.1 Temporal coupling strategy and its Firedrake implementation

In this section, we introduce the first-order symplectic Euler (SE) scheme developed for advancing the deep-water variables (h and ψ_i) and shallow-water variables (h and hu) from time step t^n to $t^{n+1} = t^n + \Delta t$. We also present its implementation in Firedrake. We end with a discussion on the time step restriction. In the SE scheme, the coupling boundary conditions and the shallow-water HLL flux are evaluated explicitly. This allows for a fully explicit coupling between the deep- and shallow-water systems, with their respective solutions updated separately.

Specifically, at each time step, the deep-water solution is updated first in Firedrake, based on the weak formulations (46) and (47), using the symplectic Euler time integration scheme, which consists of two steps.

In the first SE step, with $\delta\psi_1$ and $\delta\hat{\boldsymbol{\psi}}$ serving as test functions, respectively, the total water depth h^{n+1} and the sub-surface velocity potentials $\hat{\boldsymbol{\psi}}^*$ are updated simultaneously by *implicitly* solving the following weak formulations

$$
\begin{aligned}
&\int_0^{x_c} H_0 W^n \frac{h^{n+1}-h^n}{\Delta t}\delta\psi_1 \mathrm{d}x \\
&= \int_0^{x_c} \Bigg[\frac{L_w^2}{W^n} h^{n+1} (\delta\psi_1)_x \left(\tilde{M}_{11}\psi_{1,x}^n + \tilde{M}_{1N}^T \hat{\boldsymbol{\psi}}_x^* \right) + \frac{L_w^2}{W^n}\frac{(h_x^{n+1})^2}{h^{n+1}}\delta\psi_1 \left(\tilde{S}_{11}\psi_1^n + \tilde{S}_{1N}^T \hat{\boldsymbol{\psi}}^* \right) \\
&\quad + \frac{H_0^2}{h^{n+1}} \Big(\frac{L_w^2}{W^n} b_x^2 + W^n \Big) \delta\psi_1 \left(\tilde{A}_{11}\psi_1^n + \tilde{A}_{1N}^T \hat{\boldsymbol{\psi}}^* \right) \\
&\quad + \frac{L_w^2}{W^n} \frac{2H_0 b_x h_x^{n+1}}{h^{n+1}} \delta\psi_1 \left(\tilde{C}_{11}\psi_1^n + \tilde{C}_{1N}^T \hat{\boldsymbol{\psi}}^* \right) \\
&\quad - \frac{L_w^2}{W^n} H_0 b_x \Big[\left(\tilde{B}_{11}\psi_{1,x}^n + (\hat{\boldsymbol{\psi}}_x^*)^T \tilde{B}_{N1} \right) \delta\psi_1 + (\delta\psi_1)_x \left(\tilde{B}_{11}\psi_1^n + \tilde{B}_{1N}^T \hat{\boldsymbol{\psi}}^* \right) \Big] \\
&\quad - \frac{L_w^2}{W^n} h_x^{n+1} \Big[\left(\tilde{D}_{11}\psi_{1,x}^n + (\hat{\boldsymbol{\psi}}_x^*)^T \tilde{D}_{N1} \right) \delta\psi_1 + (\delta\psi_1)_x \left(\tilde{D}_{11}\psi_1^n + \tilde{D}_{1N}^T \hat{\boldsymbol{\psi}}^* \right) \Big] \\
&\quad - H_0 X\, \tilde{R}_t^n\, h_x^{n+1} \delta\psi_1 \Bigg] \mathrm{d}x + \left\{ L_w \tilde{R}_t^n h^{n+1} \delta\psi_1 \tilde{I}_1 \right\}\Big|_{x=0} - \left\{ L_w (hu)^n \delta\psi_1 \tilde{I}_1 \right\}\Big|_{x=x_c},
\end{aligned}
\tag{56a}
$$

and

$$
\begin{aligned}
0 = \int_0^{x_c} \Bigg[& \frac{L_w^2}{W^n} h^{n+1} \left(\psi_{1,x}^n \tilde{M}_{1N}^T + (\hat{\boldsymbol{\psi}}_x^*)^T \tilde{M}_{NN} \right) (\delta\hat{\boldsymbol{\psi}})_x \\
& + \frac{L_w^2}{W^n} \frac{(h_x^{n+1})^2}{h^{n+1}} \left(\psi_1^n \tilde{S}_{1N}^T + (\hat{\boldsymbol{\psi}}^*)^T \tilde{S}_{NN} \right) \delta\hat{\boldsymbol{\psi}} \\
& + \frac{H_0^2}{h^{n+1}} \Big(\frac{L_w^2}{W^n} b_x^2 + W^n \Big) \left(\psi_1^n \tilde{A}_{1N}^T + (\hat{\boldsymbol{\psi}}^*)^T \tilde{A}_{NN} \right) \delta\hat{\boldsymbol{\psi}} \\
& + \frac{L_w^2}{W^n} \frac{2H_0 b_x h_x^{n+1}}{h^{n+1}} \left(\psi_1^n \tilde{C}_{1N}^T + (\hat{\boldsymbol{\psi}}^*)^T \tilde{C}_{NN} \right) \delta\hat{\boldsymbol{\psi}} \\
& - \frac{L_w^2}{W^n} H_0 b_x \Big[(\delta\hat{\boldsymbol{\psi}})_x^T \left(\tilde{B}_{N1}\psi_1^n + \tilde{B}_{NN}\hat{\boldsymbol{\psi}}^* \right) + \left(\psi_{1,x}^n \tilde{B}_{1N}^T + (\hat{\boldsymbol{\psi}}_x^*)^T \tilde{B}_{NN} \right) \delta\hat{\boldsymbol{\psi}} \Big]
\end{aligned}
$$

$$
\begin{aligned}
&- \frac{L_w^2}{W^n} h_x^{n+1} \Big[(\delta \hat{\boldsymbol{\psi}})_x^T \left(\tilde{D}_{N1} \psi_1^n + \tilde{D}_{NN} \hat{\boldsymbol{\psi}}^* \right) + \left(\psi_{1,x}^n \tilde{D}_{1N}^T + (\hat{\boldsymbol{\psi}}_x^*)^T \tilde{D}_{NN} \right) \delta \hat{\boldsymbol{\psi}} \Big] \Big] \mathrm{d}x \\
&+ \left\{ L_w \tilde{R}_t^n h^{n+1} (\delta \hat{\boldsymbol{\psi}})^T \tilde{I}_N \right\} \Big|_{x=0} - \left\{ L_w (hu)^n (\delta \hat{\boldsymbol{\psi}})^T \tilde{I}_N \right\} \Big|_{x=x_c} . \qquad (56b)
\end{aligned}
$$

In the second SE substep, using δh as the test function, the free-surface potential ψ^{n+1} is updated by *explicitly* solving the weak formulation:

$$
\begin{aligned}
&\int_0^{x_c} H_0 (W^{n+1} \psi_1^{n+1}) \, \delta h \, \mathrm{d}x = \int_0^{x_c} H_0 (W^n \psi_1^n) \, \delta h \, \mathrm{d}x \\
&- \Delta t \int_0^{x_c} \Bigg[\frac{1}{2} \frac{L_w^2}{W^n} \delta h \left[\psi_{1,x}^n \tilde{M}_{11} \psi_{1,x}^n + \left(2 \psi_{1,x}^n \tilde{M}_{1N}^T + (\hat{\boldsymbol{\psi}}_x^*)^T \tilde{M}_{NN} \right) \hat{\boldsymbol{\psi}}_x^* \right] \\
&+ \frac{L_w^2}{W^n} \left(\frac{h_x^{n+1} (\delta h)_x}{h^{n+1}} - \frac{\delta h (h_x^{n+1})^2}{2 (h^{n+1})^2} \right) \left[\psi_1^n \tilde{S}_{11} \psi_1^n + \left(2 \psi_1^n \tilde{S}_{1N}^T + (\hat{\boldsymbol{\psi}}^*)^T \tilde{S}_{NN} \right) \hat{\boldsymbol{\psi}}^* \right] \\
&- \frac{H_0^2}{2 (h^{n+1})^2} \delta h \left(\frac{L_w^2}{W^n} b_x^2 + W^n \right) \left[\psi_1^n \tilde{A}_{11} \psi_1^n + \left(2 \psi_1^n \tilde{A}_{1N}^T + (\hat{\boldsymbol{\psi}}^*)^T \tilde{A}_{NN} \right) \hat{\boldsymbol{\psi}}^* \right] \\
&+ \frac{L_w^2}{W^n} \frac{H_0 b_x}{h^{n+1}} \left((\delta h)_x - \frac{\delta h \, h_x^{n+1}}{h^{n+1}} \right) \left[\psi_1^n \tilde{C}_{11} \psi_1^n + \left(2 \psi_1^n \tilde{C}_{1N}^T + (\hat{\boldsymbol{\psi}}^*)^T \tilde{C}_{NN} \right) \hat{\boldsymbol{\psi}}^* \right] \\
&- \frac{L_w^2}{W^n} (\delta h)_x \left[\left(\tilde{D}_{11} \psi_{1,x}^n + (\hat{\boldsymbol{\psi}}_x^*)^T \tilde{D}_{N1} \right) \psi_1^n + \left(\psi_{1,x}^n \tilde{D}_{1N}^T + (\hat{\boldsymbol{\psi}}_x^*)^T \tilde{D}_{NN} \right) \hat{\boldsymbol{\psi}}^* \right] \\
&+ H_0 \left(g W^n \delta h (h^{n+1} - H) - \psi_1^n X \tilde{R}_t^n (\delta h)_x \right) \Bigg] \mathrm{d}x \\
&- \Delta t \left\{ L_w \tilde{R}_t^n \left(\psi_1^n \tilde{I}_1 + (\hat{\boldsymbol{\psi}}^*)^T \tilde{I}_N \right) \delta h \right\} \Big|_{x=0} \\
&- \Delta t \left\{ L_w \frac{(hu)^n}{h^{n+1}} \left(\psi_1^n \tilde{G}_1 + (\hat{\boldsymbol{\psi}}^*)^T \tilde{G}_N \right) \delta h \right\} \Bigg|_{x=x_c} . \qquad (57)
\end{aligned}
$$

After the deep-water update, the shallow-water solution is advanced using the updated values from the deep-water side at the coupling boundary $x = x_c$. Specifically, the shallow-water coupling boundary condition (55) at $x = x_c = x_{-1/2}$ is imposed as follows:

$$
h_{-1/2}^{n+1} = \left\{ h^{n+1} \right\} \Big|_{x=x_c} , \qquad (58a)
$$

$$
\begin{aligned}
(hu)_{-1/2}^* = \frac{1}{H_0} \Big\{ & h^{n+1} \left(\psi_{1,x}^n \tilde{I}_1 + (\hat{\boldsymbol{\psi}}^*)^T \tilde{I}_N \right) - h_x^{n+1} \left(\psi_1^n \tilde{G}_1 + (\hat{\boldsymbol{\psi}}^*)^T \tilde{G}_N \right) \\
& - H_0 b_x \left(\psi_1^n \tilde{J}_1 + (\hat{\boldsymbol{\psi}}^*)^T \tilde{J}_N \right) \Big\} \Big|_{x=x_c} , \qquad (58b)
\end{aligned}
$$

where the column vector $\tilde{J}$ is defined as $\tilde{J}_i = \int_0^{H_0} \frac{\mathrm{d}\tilde{\varphi}_i}{\mathrm{d}z} \, \mathrm{d}z$.

The shallow-water variables h and hu are then updated according to

$$
h_k^{n+1} = h_k^n - \frac{\Delta t}{\Delta x_S} \left(F_{k+1/2}^h - F_{k-1/2}^h \right) , \qquad (59a)
$$

$$(hu)_k^{n+1} = (hu)_k^n - \frac{\Delta t}{\Delta x_S}\left[\left(F_{k+1/2}^{hu} - F_{k-1/2}^{hu}\right) - \frac{1}{2}g\left((h_{k+1/2}^{n+1})^2 - (h_{k-1/2}^{n+1})^2\right)\right], \tag{59b}$$

where the Harten–Lax–van Leer (HLL) flux is used to compute the numerical fluxes F^h and F^{hu}, defined by

$$\mathbf{F}(\mathbf{U}) = \begin{pmatrix} hu \\ hu^2 + \frac{1}{2}gh^2 \end{pmatrix} \equiv \begin{pmatrix} F^h \\ F^{hu} \end{pmatrix}. \tag{60}$$

For the shallow-water depth h, the numerical flux is computed explicitly as

$$F_{k+1/2}^h = \begin{cases} 0 & \text{if } S_L = S_R = 0, \\ F_-^h & \text{if } S_L > 0, \\ F_+^h & \text{if } S_R < 0, \\ \dfrac{S_R^h F_-^h - S_L^h F_+^h + S_L^h S_R^h\left(h_{(k+1/2)^+}^n - h_{(k+1/2)^-}^n\right)}{S_R^h - S_L^h} & \text{otherwise,} \end{cases}$$

where the left and right fluxes $F_\pm^h$ at the cell interface $x = x_{k+1/2}$ are evaluated as

$$F_-^h \equiv (hu)_{(k+1/2)^-}^n = h_{(k+1/2)^-}^n u_k^n, \tag{61a}$$

$$F_+^h \equiv (hu)_{(k+1/2)^+}^n = h_{(k+1/2)^+}^n u_{k+1}^n, \tag{61b}$$

with $u_k^n = (hu)_k^n / h_k^n$. The locally constructed shallow-water depths $h_{(k+1/2)^\pm}^n$ are given by (B7). The left and right wave speeds are explicitly computed as

$$S_L^h = \min\left\{\left[\frac{(hu)^n}{h^n} - \sqrt{gh^n}\right]_{(k+1/2)^-}, \left[\frac{(hu)^n}{h^n} - \sqrt{gh^n}\right]_{(k+1/2)^+}\right\}, \tag{62a}$$

$$S_R^h = \max\left\{\left[\frac{(hu)^n}{h^n} + \sqrt{gh^n}\right]_{(k+1/2)^-}, \left[\frac{(hu)^n}{h^n} + \sqrt{gh^n}\right]_{(k+1/2)^+}\right\}. \tag{62b}$$

Given the updated h_k^{n+1}, the other shallow-water variable hu is updated in a semi-explicit manner. The flux for hu is evaluated using the HLL scheme, where the flux function depends on the newly updated h^{n+1} and the old velocity-like variable $(hu)^n/h^n$. The numerical flux reads

$$F_{k+1/2}^{hu} = \begin{cases} 0 & \text{if } S_L = S_R = 0, \\ F_-^{hu} & \text{if } S_L > 0, \\ F_+^{hu} & \text{if } S_R < 0, \\ \dfrac{S_R^{hu} F_-^{hu} - S_L^{hu} F_+^{hu} + S_L^{hu} S_R^{hu}\left((hu)_{(k+1/2)^+}^n - (hu)_{(k+1/2)^-}^n\right)}{S_R^{hu} - S_L^{hu}} & \text{else,} \end{cases}$$

where the left and right fluxes $F_{\pm}^{hu}$ evaluated at cell interface $x = x_{k+1/2}$ are computed as

$$F_{\pm}^{hu} \equiv \left[\frac{((hu)^n)^2}{h^{n+1}} + \frac{1}{2} g (h^{n+1})^2 \right]_{(k+1/2)^{\pm}}. \tag{63}$$

Here, the updated depth h^{n+1} enters the pressure term and denominator to improve numerical stability and consistency with the mass update. The corresponding wave speeds are estimated using the velocity at time level n and the updated depth:

$$S_L^{hu} = \min \left\{ \left[\frac{(hu)^n}{h^n} - \sqrt{g h^{n+1}} \right]_{(k+1/2)^-}, \left[\frac{(hu)^n}{h^n} - \sqrt{g h^{n+1}} \right]_{(k+1/2)^+} \right\}, \tag{64a}$$

$$S_R^{hu} = \max \left\{ \left[\frac{(hu)^n}{h^n} + \sqrt{g h^{n+1}} \right]_{(k+1/2)^-}, \left[\frac{(hu)^n}{h^n} + \sqrt{g h^{n+1}} \right]_{(k+1/2)^+} \right\}. \tag{64b}$$

This update is referred to as semi-explicit because the nonlinear flux function for hu depends on both the solution at the previous time level, $(hu)^n$, and the updated water depth h^{n+1}, which is already available from the preceding update step. By mixing time levels in this way—using h^{n+1} for stability whilst retaining $(hu)^n$ to avoid solving a fully nonlinear system—the scheme maintains an explicit time-stepping structure whilst benefiting from improved numerical robustness.

Finally, the updated $(hu)^{n+1}$ provides the coupling boundary condition in the deep-water weak formulations to be used for the next time step:

$$\left\{ (hu)^{n+1} \right\} \Big|_{x=x_c} = (hu)^{n+1}_{-1/2}. \tag{65}$$

In summary, this symplectic Euler scheme for the whole system has four steps:

1. First, update the deep-water solutions using the symplectic Euler scheme by solving the weak formulations (56) and (57).
2. Then, set the shallow-water boundary condition at $x = x_c$ with (58).
3. Next, update the shallow-water solutions using a forward-Euler scheme as per (59).
4. Finally, save the deep-water boundary condition (65) to be used for the next time step.

The scheme is faster than a strict symplectic Euler scheme, since it avoids iterations required to implicitly solve the coupling terms by explicitly evaluating the HLL-fluxes.

The time step restriction for the symplectic Euler scheme used for solving the deep-water subdomain is given by $\Delta t_D \leq 2/\omega_{\max}$, where $\omega_{\max}$ is estimated based on the linear dispersion relation [28]. For the finite-volume shallow-water solver, the time step Δt_S is restricted by the Courant–Friedrichs–Lewy (CFL) condition to maintain numerical stability. Given the uniform mesh size Δx_S, the CFL condition can be written as (cf. [20])

$$\Delta t_S \leq CFL \Delta x_S / \max_k \left\{ |u_k| + \sqrt{g h_k} \right\}, \tag{66}$$

Table 1 Parameters used with units given in square brackets

Domain			Beach	
L_x [m]	H_0 [m]	$H(x_c)$ [m]	x_b [m]	s_b
14.0	1.0	0.2	3.0	0.1
Wavemaker				
λ [m]	ω [rad/s]	T_w [s]	γ [m]	L_w [m]
2.0	5.54	1.13	0.02	1.0
Resolution				
Δx_D [m]	Δx_S [m]	n_z	Δt [s]	
0.05	0.0025	8	0.001	

The simulation runs from $t_0 = 0$ s to 124.72 s with wavemaker turned off at 68.04 s

where $u_k = (hu)_k/h_k$ is the horizontal velocity in cell k, and $CFL < 1$ is the Courant number. Here, $|u_k| + \sqrt{gh_k}$ represents the characteristic wave speed at each cell, accounting for both advection by the flow and gravity wave propagation. It ensures that information does not travel more than one cell during a single time step, thus maintaining numerical stability. Hence, the overall time step criterion for the coupled model becomes $\Delta t \leq \min\{\Delta t_D, \Delta t_S\}$.

4 Results

The effectiveness of the sloping beach in absorbing wave energy is investigated in the following test case. The seabed is flat when $x < x_b$, beyond which a sloping beach begins, defined by $b(x) = s_b(x - x_b)$ for $x \in [x_b, L_x]$. The wavemaker motion is prescribed as $R(t) = \gamma\cos(\omega t)$, where γ denotes the maximum displacement from $x = 0$ with oscillation period $T_w = 2\pi/\omega$. The simulation is run for $t \in [0, 110]T_w = [0, 124.73]$s, with the wavemaker motion arrested after $t = 60T_w = 68.04$s. The parameters used are found in Table 1. Short or deep-water waves roughly satisfy the relation $\lambda < 2H(x)$ with wave length λ and (rest) water depth $H(x)$ at position x in the beach region. Long shallow-water waves roughly satisfy $\lambda > 10H(x)$ to $20H(x)$. These rough estimates justify our choice of $\lambda/H(x_c) = 10$ such that for $\lambda = 2$m we find that $H(x_c) = 0.2$ and $x_c = x_b + s_b\,(H_0 - H(x_c)) = 11$m for a beach slope of $s_b = 0$ and the beach starting at $x_b = 3$m. During or after the simulations, we also visually check whether the velocity potential $\phi(x, z, t)$ displays sufficient depth independence, i.e. as can be discerned from Fig. 5. Further discussion is found in [5], wherein two simulations with the MSA are compared for different values of x_c, ones with $\lambda/H(x_c) = 5, 12.5$; a difference seen to lead to only minor changes in the results.

To assess the efficacy of the sloping beach in dissipating wave energy, we compute and display energy variations in both deep- and shallow-water subdomains, in Fig. 4. These energies are offset by their initial rest values at $t_0 = 0$ s, cf. Fig. 5a.

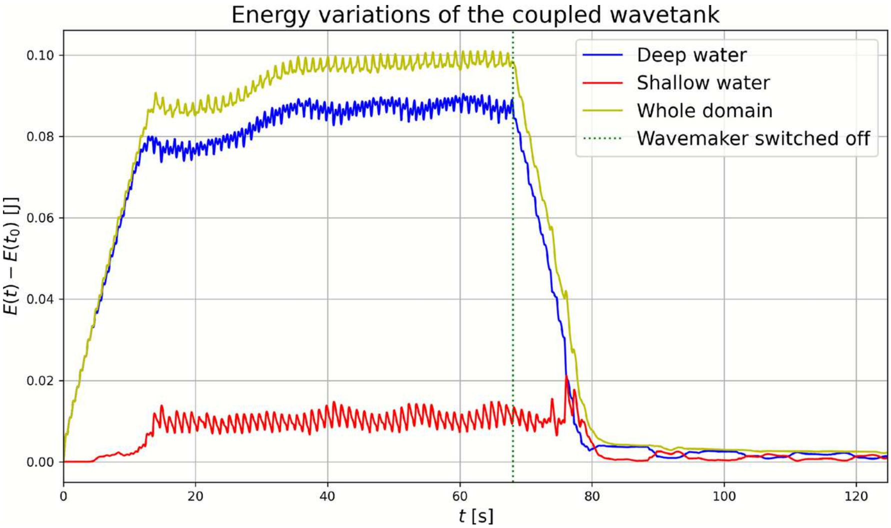

Fig. 4 Energy variations in the coupled wavetank with energies of deep-water and shallow-water subdomains, and the total energy in the full domain, shown in blue, red, and yellow, respectively. The wavemaker is switched off at $t = t_{\text{stop}} = 68.04$ s as marked by a vertical dotted green line. (Color figure online)

Immediately after the wavemaker is activated, energy is on average put into the system. It results in a steady increase in the total energy, most of which accumulates in the deep-water region. The onset of energy growth in the shallow-water region is delayed, beginning around $t \approx 4.4$ s—the time required for waves to propagate across the deep-water subdomain and reach the shallow-water region (cf. Fig. 5b). At this point, the shallow-water energy begins to rise, whilst a slight reduction in the gradient of the deep-water energy curve indicates energy transfer across the coupling interface. From this point onward, the total energy continues to increase, implying that the rate of energy put in by the wavemaker exceeds the rate of dissipation on the beach. The consistent slope of the total energy curve during this phase suggests a smooth and effective transmission of energy from the deep-water to the shallow-water region via the coupling interface.

Around $t \approx 36$ s, the system appears to reach a *dynamic equilibrium*, where the total energy oscillates around a nearly constant value. This plateau indicates that the energy input from the wavemaker is now approximately balanced by the dissipation mechanisms in the shallow-water region. During this equilibrium phase, the wave field is fully developed (cf. Fig. 5c), characterised by regular wave propagation in the deep-water region and wave shoaling, cresting, and wave breaking on the beach slope.

The energy dissipation on the sloping beach is achieved through bore formation and shoaling in the surf zone, as illustrated in a series of snapshots taken over one wavemaker period, $t \in [59, 60]T_w$, in Fig. 6. At $t = 59T_w$, a bore begins to form near the coupling interface. It then propagates towards the dry beach, with its front becoming steeper whilst its amplitude gradually decreases, until it eventually breaks and is fully absorbed by the beach at $t = 60T_w$. At this point, the situation closely

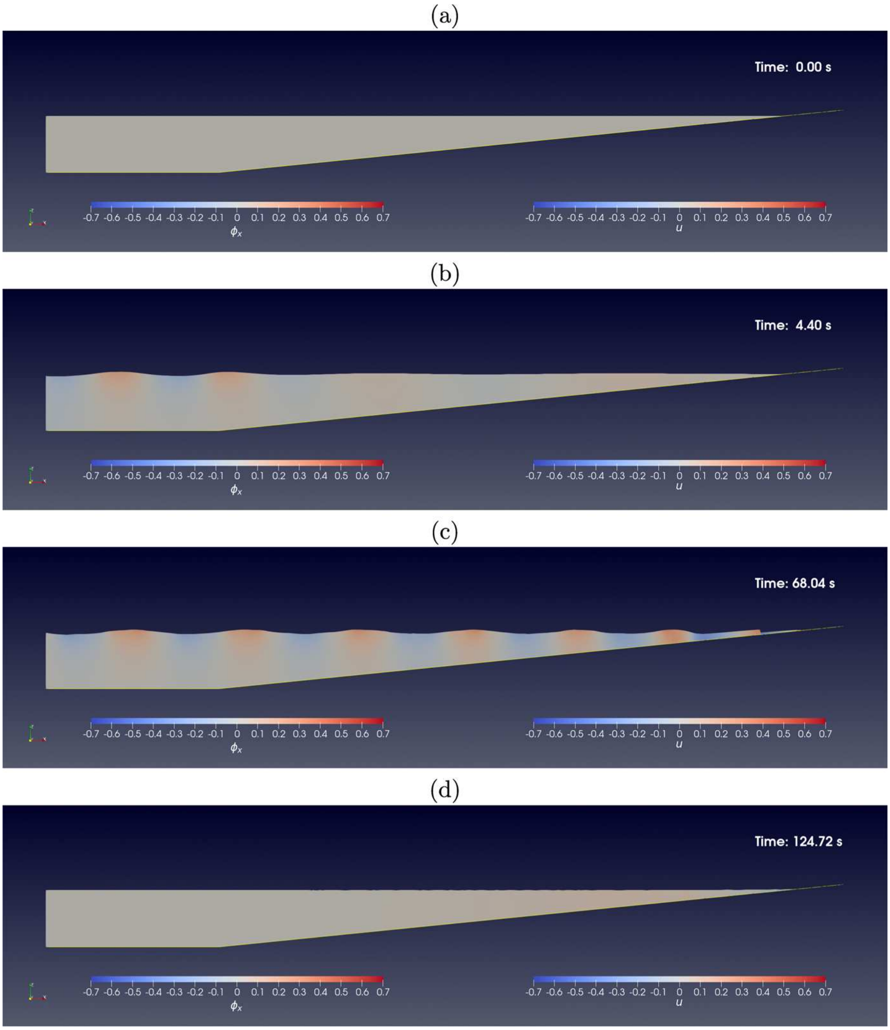

Fig. 5 Wave motions in the coupled wavetank at different times. **a** Water at rest at initial time $t = t_0 = 0\,\mathrm{s}$. **b** Waves propagate through the deep-water region and begin to enter the shallow-water region at $t \approx 4.4\,\mathrm{s}$, marked by a rise in shallow-water energy. **c** Fully developed water waves in the wavetank at $t = t_{\mathrm{stop}} = 68.04\,\mathrm{s}$. Energy input from the wavemaker balances dissipation at the beach, reaching dynamic equilibrium. **d** Remaining waves in the wavetank at $t = t_{\mathrm{end}} = 124.72\,\mathrm{s}$ due to wave reflections between the solid boundaries. Note that Horizontal velocities ($u = \phi_x$ in deep water and $u = hu/h$ in shallow water) are shown in the same legend range across the whole domain. A video covering the full simulation is available at https://youtu.be/HFw2ayh2oXk?si=7OxCHZ_u1LEku_eN

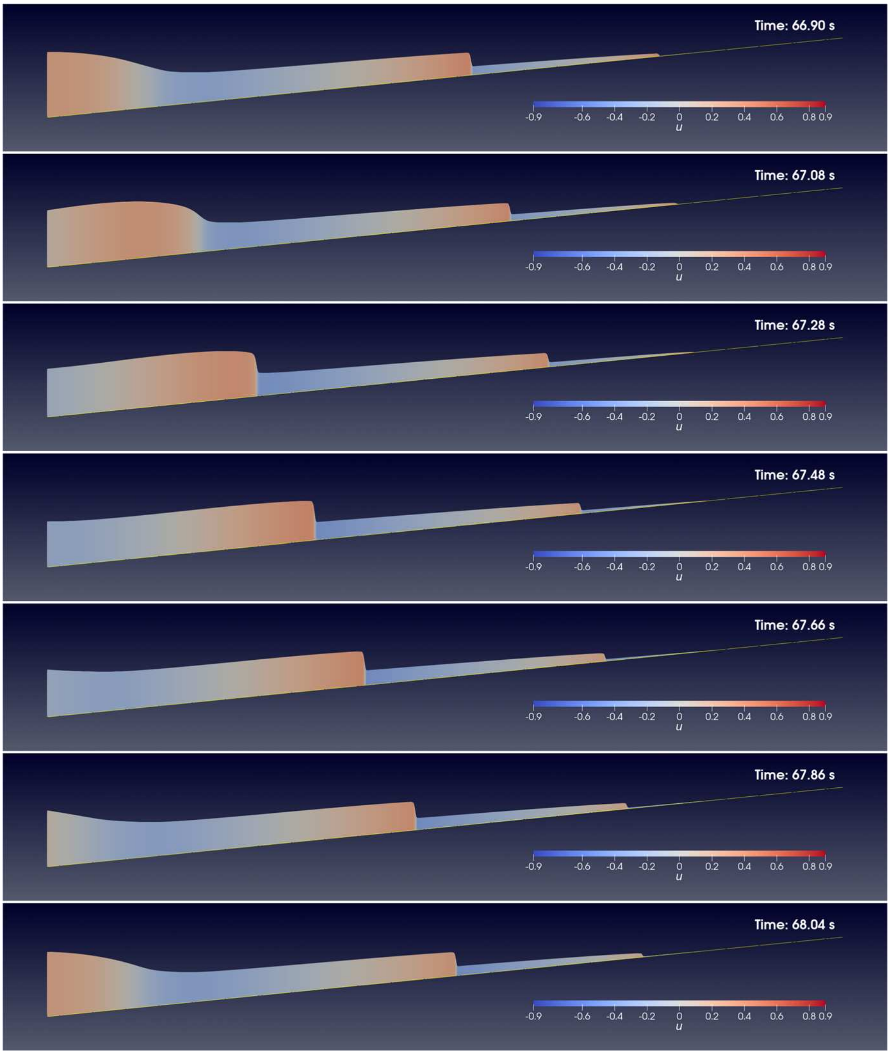

Fig. 6 Wave shoaling and bore formation in the shallow-water subdomain. Temporal snapshots are captured for one period $t \in [59, 60]T_w = [66.90, 68.04]$ s, whilst the coupled wavetank remains in the dynamic equilibrium state. The colour legend indicates the horizontal velocity u in the shallow-water domain

resembles the beginning of the period at $t = 59T_w$, with a new bore once again starting to form near the coupling interface.

To verify that most of the input energy is absorbed by the beach, the wavemaker is switched off at $t = t_{\text{stop}} = 68.04$ s, as marked by the green dotted vertical line in Fig. 4. Immediately after this shutdown, the total energy decreases rapidly at an on average (negative) rate similar to its initial (positive) rate. Due to the time required for the final group of waves to traverse the deep-water region, a delay is observed before the shallow-water energy begins to decrease. The energy curves show that the total

Table 2 Parameters used for the simulations examining the effect of the mild-slope approximation. Units are given in square brackets

Whole domain			Beach	
L_x [m]	H_0 [m]	$H(x_c)$ [m]	x_b [m]	s_b
10.0	1.0	0.2	4.0	0.2
Wavemaker				
λ [m]	ω [rad/s]	T_w [s]	γ [m]	L_w [m]
2.0	5.54	1.13	0.03	1.0
Resolutions				
Δx_D [m]	Δx_S [m]	n_z	Δt [s]	
0.05	0.0025	8	0.001	

energy does not return to zero by the end of the simulation at $t = 110T_w$, because small long-wave residual waves remain, reflecting between the solid boundaries, and the water has not yet come to complete rest—as seen in the nonzero velocities in Fig. 5d. The oscillations in Fig. 4 are on the timescale of the wavemaker with a period $T_w = 1.13$s. Note that they are also present in the first circa 12s of net gross energy input when the waves do not yet dissipate at the beach due to wave breaking and that they gradually disappear after the wavemaker is switched off.

The remaining total energy, averaged over $t \in [105, 110]T_w$, is $\bar{E}_2 = 0.0024$ J, which accounts for 2.4% of the total energy at the dynamic equilibrium state, $\bar{E}_1 = 0.0987$ J, averaged over $t \in [55, 60]T_w$. This demonstrates that the numerical wavetank, coupled with an absorbing beach, successfully fulfils its intended purpose in the present model.

Next, to quantitatively examine the effect of the mild-slope approximation (MSA), two simulations were performed—one using the full weak formulations (FWF) and coupling conditions, whilst the other MSA formulation ignores all kinetic energy terms containing b_x in the model formulation. The configurations for the two simulations are otherwise identical, and they are summarised in Table. 2. In this case, the beach slope is set to $s_b = 0.2$ and the amplitude of the wavemaker motion is $\gamma = 0.03$, which are larger than those in the previous test, with the expectation that these conditions will better highlight the differences between the two setups. Both FWF and MSA simulations run from $t_0 = 0$ s to $t_{\text{end}} = 20T_w = 22.68$ s, with the wavemaker turned off at $t_{\text{stop}} = 10T_w = 11.34$ s. Note that the differences in runtime are negligible.

In the deep-water subdomain, the horizontal velocity $u = \phi_x$ varies in the range $[-0.452, 0.793]$ for the case where MSA is not applied, whereas for the case using MSA, it falls within the range $[-0.437, 0.746]$, which is smaller than the former. The sloping beach in FWF causes the wave motion to intensify slightly, as observed in the evolution of water depth and velocity evaluated at the coupling point, denoted by h_c and u_c respectively, shown in Fig. 7a. The wave amplitude and velocity tend to be higher in the FWF case. These differences become more noticeable after the wavemaker stops, with the maximum relative difference for h_c and u_c reaching 3.21% and 12.0%, respectively. A comparison of the artificial $h = 0$-waterline position $x_w(t)$

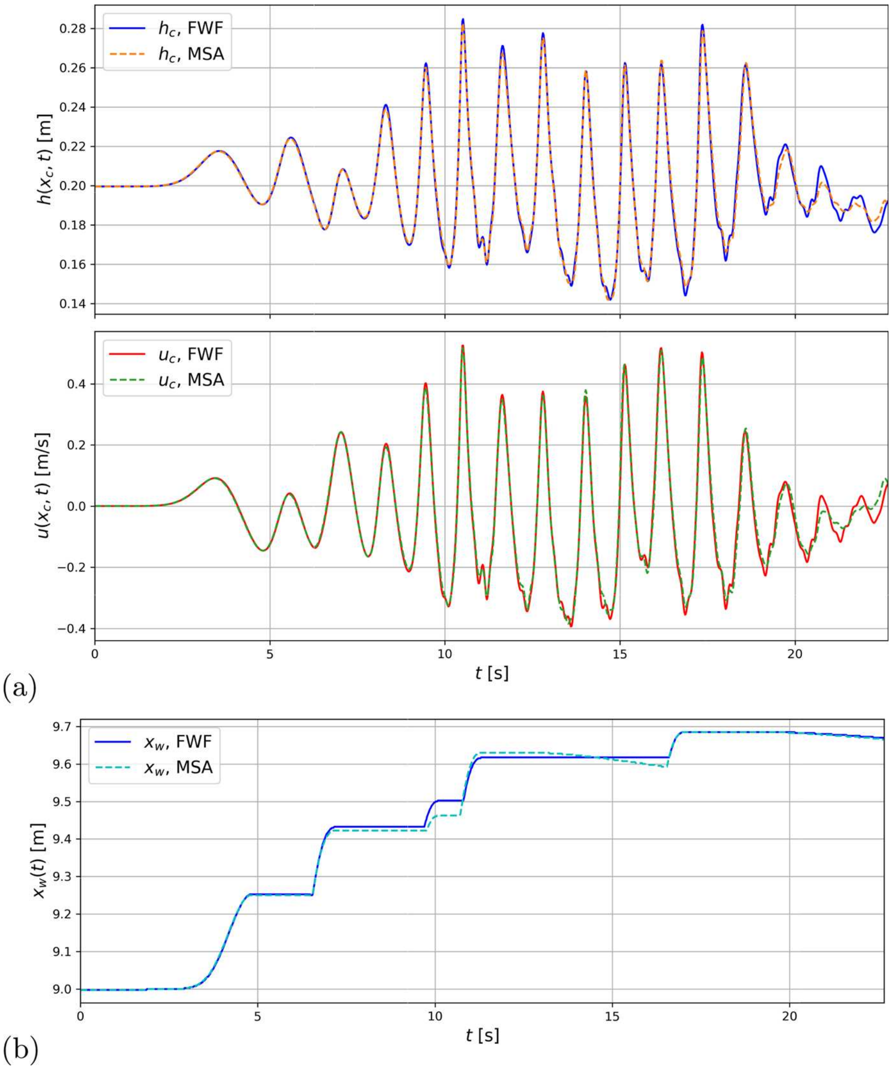

Fig. 7 Effect of the mild-slope approximation (MSA) on the selected solutions. Numerical results obtained using full weak formulations (FWF) and coupling conditions are represented by solid lines, whilst those from MSA are shown as dashed lines. **a** Evolution of water depth $h(x_c, t)$ and horizontal velocity $u(x_c, t)$ evaluated at the coupling point. **b** Evolution of "$h = 0$-waterline position" $x_w(t)$

is carried out in Fig. 7b. The maximum relative difference is seen to occur at $t = 9.98$ s. Hence, the effect of the mild-slope approximation is not negligible. This underscores the need to revisit the validations against experimental test cases [5], where the MSA was used. Better agreement is expected to be achieved with the present improved model.

Due to the numerical wetting-and-drying algorithm of [20] employed, the determination of a waterline position $x_w(t)$ is ambiguous. In Fig. 8, we therefore analyse

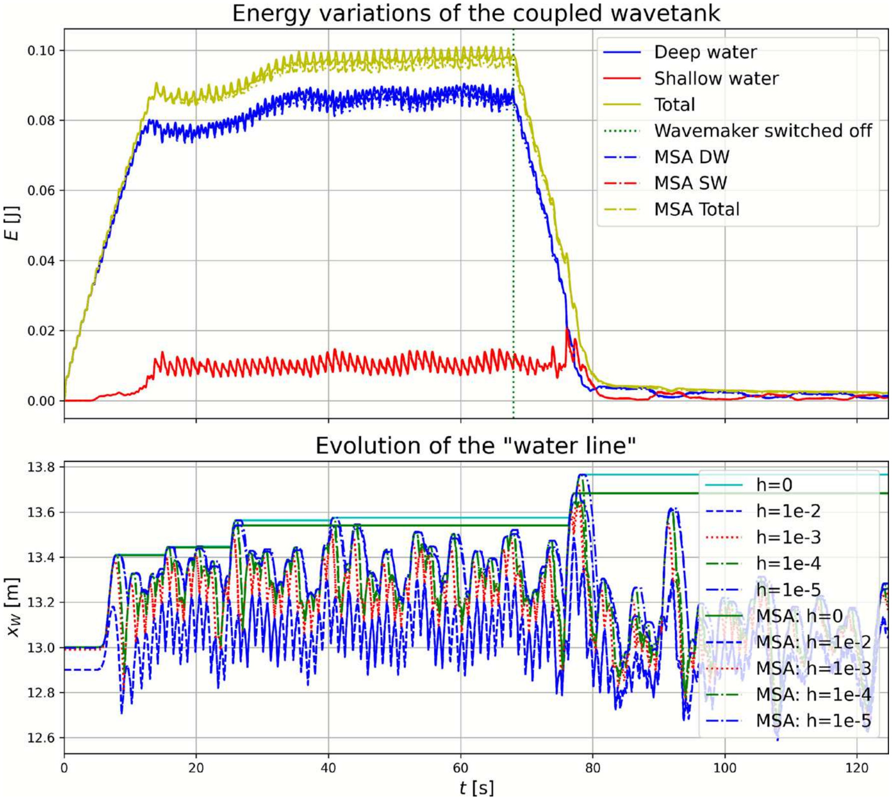

Fig. 8 Analysis and determination of a waterline. Top: Energies in MSA and FWF are largely similar with total MSA energy slightly smaller. Bottom: approximate determination of waterline position

the dynamics by defining various "waterline" points defined by (the right-most) water depths $h = 0, 0.01, 10^{-3}, 10^{-4}, 10^{-5}$ for both MSA and FWF. The mathematical waterline should oscillate back and forth on the sloping beach, which appears to be captured by a cut-off level $h \approx 10^{-4}, 10^{-5}$.

Code performance, both in terms of computation speed and memory usage, has improved following an upgrade of wavemaker-related functions in the time loop. Specifically, a Firedrake `Constant` object is used to hold the time value in the expressions for these wavemaker-related functions, instead of directly using the time variable `t` [7]. By updating the `Constant` at each time step, the symbolic expressions do not need to be regenerated, thereby avoiding the request for new memory and saving a significant amount of time [7]. After this improvement, the long-time simulation ($t \in [0, 110]T_w = [0, 124.73]$ s, nearly 1.24×10^5 time steps with $\Delta t = 10^{-3}$ s, and DoFs $= (N_e + 1)(n_z + 1) + N_v = 3189$) took 1 : 27hr to complete in a serial computation on a 2020 MacBook Pro, with memory usage 300–400MB. It makes this numerical wavetank a *cost-effective* tool for practical problems in the maritime industry.

5 Conclusion and discussion

We have presented the first numerical wavetank with fully nonlinear coupling between deep-water (potential-flow) and shallow-water equations using a variational approach. The variational approach ensured stable simulations of waves travelling through the coupling interface Γ_c in a smooth way, resulting in (nearly) uni-directional waves, thereby simulating a credible (scaled-down) realistic sea state. The energy variations show that the coupling interface behaves as a transparent boundary for the deep-water waves, whilst the beach absorbs more than 97% of the energy. The model may therefore be used as a cost-improved alternative of a deep-water model, such as the ones presented in [5, 7] and [29], since it reduces the size of the numerical domain and thereby saves substantial computational resources. The choice of absorbing waves with a topographical beach makes the numerical tank similar to experimental wave tanks, e.g. the one at MARIN, wherein waves are generated by a (piston) wavemaker and absorbed through wave breaking on the beach. Wave generation can thus first be tested in our numerical wave tank before being used in experimental set-ups, thereby ensuring that the wavemaker motion will by design generate the waves in the target area, which is of practical value.

Some improvements can increase the efficiency of the present numerical tank, as follows. First, the semi-symplectic Euler scheme used for optimal computational cost may be extended to the symplectic Euler scheme or a higher-order scheme by dealing with the implicit evaluation of the HLL flux in shallow water. For instance, the second-order Störmer-Verlet scheme implemented in [5, 7] in deep water may be applied to the coupled model or the modified mid-point method (as implemented variationally in [29]). Second, the implementation of the shallow-water solver is not yet optimised and could be improved by parallel computing; on which note, the deep-water solver may be compiled in parallel without any additional modification, cf. the automatic parallelisation features in Firedrake [30, 31]. Third, the coupling location is chosen *a priori* based on the characteristic wavelengths and in situ water depth involved; though this has the advantage of being fixed and prescribed, note that it is not optimal for irregular waves. Indeed, to make sure that the vertical variations of the velocity potential are negligible at the coupling point for irregular waves dynamic determination of x_c can be made depending on the vertical structure of the velocity potential in the potential-flow domain, thus ensuring that the shallow-water assumption holds at the coupling point. Another solution was developed by Cotter and Bokhove [32] and extended by Gagarina et al. [25], who proposed a new model that encompasses both the three-dimensional potential-flow water-water model and the depth-averaged shallow-water model as limiting systems. Consequently, the coupling point sets itself dynamically; both Cotter and Bokhove [32] and Gagarina et al. [25] also derive hydraulic-jump conditions for this new model, which conditions equal the usual shallow-water ones in the shallow-water limit. An extension of the present model to a 3D tank is also possible. Since (i) the 3D deep-water model has been implemented in [5–7] and [29], and (ii) the surface shallow-water model is part of Flooddrake in Firedrake [33], the extension of the coupling to a two-dimensional interface in 3D comprises future work.

Finally, we aim to validate the coupled model against wave-beach experiments with regular and irregular wave trains, e.g. those made at the Delft University of Technology, as described in [5], including preliminary validations using the model with the MSA.

Appendix A Discrete coupling conditions

The coupling conditions at $x = x_c$ for the deep- and shallow-water subdomains originate from the following terms in the continuous variational principle (4):

$$\left\{\int_b^{b+h} \delta\phi\, \phi_x \,\mathrm{d}z\right\}\Big|_{x=x_c} - \left\{\delta\check{\phi}\big(h\,\check{\phi}_x\big)\right\}\Big|_{x=x_c}. \tag{A1}$$

To derive the explicit, discrete coupling condition for the deep-water region, we use the relation (10), so that (A1) becomes

$$\left\{\int_b^{b+h} \delta\phi\, \phi_x \,\mathrm{d}z\right\}\Big|_{x=x_c} - \left\{\frac{hu}{h}\int_b^{b+h} \delta\phi \,\mathrm{d}z\right\}\Big|_{x=x_c}, \tag{A2}$$

where $u \equiv \check{\phi}_x$ has been substituted. Applying the coordinate transformation (15), this expression becomes

$$\begin{aligned}&\left\{\int_b^{b+h} \delta\phi\Big(\phi_x - \frac{hu}{h}\Big)\mathrm{d}z\right\}\Big|_{x=x_c}\\ \to\ &\left\{\int_0^{H_0}\Big(-\frac{z}{h}\phi_z\delta h + \delta\phi\Big)\left(\frac{L_w}{W}\phi_x - \frac{L_w(zh_x + H_0 b_x)}{Wh}\phi_z - \frac{hu}{h}\right)\frac{h}{H_0}\,\mathrm{d}z\right\}\Big|_{x=x_c}.\end{aligned} \tag{A3}$$

Substituting the vertical expansion $\phi(x,z,t) = \psi_i(x,t)\,\tilde{\varphi}_i(z)$ into the transformed expression, the transformed coupling term can be computed as

$$\begin{aligned}&\left\{\int_0^{H_0}\Big(-\frac{z}{h}\psi_j\,\tilde{\varphi}_{j,z}\delta h + \delta\psi_j\,\tilde{\varphi}_j\Big)\left(\frac{L_w}{W}\psi_{i,x}\tilde{\varphi}_i - \frac{L_w(zh_x + H_0 b_x)}{Wh}\psi_i\,\tilde{\varphi}_{i,z} - \frac{hu}{h}\right)\frac{h}{H_0}\,\mathrm{d}z\right\}\Big|_{x=x_c}\\
=\ &\left\{-\int_0^{H_0}\delta h\frac{z}{H_0}\psi_j\,\tilde{\varphi}_{j,z}\left(\frac{L_w}{W}\psi_{i,x}\tilde{\varphi}_i - \frac{L_w(zh_x + H_0 b_x)}{Wh}\psi_i\,\tilde{\varphi}_{i,z} - \frac{hu}{h}\right)\mathrm{d}z\right\}\Big|_{x=x_c}\\
&+\left\{\int_0^{H_0}\delta\psi_j\frac{h}{H_0}\tilde{\varphi}_j\left(\frac{L_w}{W}\psi_{i,x}\tilde{\varphi}_i - \frac{L_w(zh_x + H_0 b_x)}{Wh}\psi_i\,\tilde{\varphi}_{i,z} - \frac{hu}{h}\right)\mathrm{d}z\right\}\Big|_{x=x_c}\\
=\ &\left\{\delta h\frac{1}{H_0}\frac{hu}{h}\psi_j\int_0^{H_0} z\,\tilde{\varphi}_{j,z}\,\mathrm{d}z\right\}\Big|_{x=x_c} - \left\{\delta h\frac{L_w}{H_0 W}\psi_{i,x}\int_0^{H_0} z\tilde{\varphi}_i\tilde{\varphi}_{j,z}\,\mathrm{d}z\,\psi_j\right\}\Big|_{x=x_c}\\
&+\left\{\delta h\frac{L_w}{WH_0}\frac{h_x}{h}\psi_i\int_0^{H_0} z^2\tilde{\varphi}_{i,z}\,\tilde{\varphi}_{j,z}\,\mathrm{d}z\,\psi_j\right\}\Big|_{x=x_c} + \left\{\delta h\frac{L_w}{W}\frac{b_x}{h}\psi_i\int_0^{H_0} z\tilde{\varphi}_{i,z}\,\tilde{\varphi}_{j,z}\,\mathrm{d}z\,\psi_j\right\}\Big|_{x=x_c}\\
&-\left\{\delta\psi_j\frac{hu}{H_0}\int_0^{H_0}\tilde{\varphi}_j\,\mathrm{d}z\right\}\Big|_{x=x_c} + \left\{\delta\psi_j\frac{hL_w}{WH_0}\psi_{i,x}\int_0^{H_0}\tilde{\varphi}_i\tilde{\varphi}_j\,\mathrm{d}z\right\}\Big|_{x=x_c}\\
&-\left\{\delta\psi_j\frac{L_w h_x}{WH_0}\psi_i\int_0^{H_0} z\tilde{\varphi}_{i,z}\,\tilde{\varphi}_j\,\mathrm{d}z\right\}\Big|_{x=x_c} - \left\{\delta\psi_j\frac{L_w b_x}{W}\psi_i\int_0^{H_0}\tilde{\varphi}_{i,z}\,\tilde{\varphi}_j\,\mathrm{d}z\right\}\Big|_{x=x_c}\end{aligned}$$

$$\begin{aligned} &= \left\{\delta h \frac{1}{H_0}\frac{hu}{h}\psi_j \tilde{G}_j\right\}\Big|_{x=x_c} - \left\{\delta h \frac{1}{\Upsilon}\psi_{i,x}\tilde{D}_{ij}\psi_j\right\}\Big|_{x=x_c} \\ &\quad + \left\{\delta h\frac{1}{\Upsilon}\frac{h_x}{h}\psi_i\tilde{S}_{ij}\psi_j\right\}\Big|_{x=x_c} + \left\{\delta h\frac{L_w}{W}\frac{b_x}{h}\psi_i\tilde{C}_{ij}\psi_j\right\}\Big|_{x=x_c} \\ &\quad - \left\{\delta\psi_j\frac{hu}{H_0}\tilde{I}_j\right\}\Big|_{x=x_c} + \left\{\delta\psi_j\frac{h}{\Upsilon}\psi_{i,x}\tilde{M}_{ij}\right\}\Big|_{x=x_c} \\ &\quad - \left\{\delta\psi_j\frac{h_x}{\Upsilon}\psi_i\tilde{D}_{ji}\right\}\Big|_{x=x_c} - \left\{\delta\psi_j\frac{L_w b_x}{W}\psi_i\tilde{B}_{ji}\right\}\Big|_{x=x_c}. \end{aligned}$$

The results are consistent with the boundary terms at $x = x_c$ collected from (22) and (24). Using the relations $\Upsilon|_{x=x_c} = H_0$ and $W|_{x=x_c} = L_w$ and with $i, j \in [1, n_z + 1]$, the transformed z-discretised coupling conditions for the deep-water domain (cf. the continuous formulation (11)) emerge as

$$\delta h|_{x=x_c}: \quad \frac{1}{H_0}\Big(\psi_{i,x}\tilde{D}_{ij}\psi_j - \frac{h_x}{h}\psi_i\tilde{S}_{ij}\psi_j\Big) - \frac{b_x}{h}\psi_i\tilde{C}_{ij}\psi_j = \frac{1}{H_0}\frac{hu}{h}\psi_j\tilde{G}_j, \tag{A4a}$$

$$\delta\psi_j|_{x=x_c}: \quad \frac{1}{H_0}\Big(h\psi_{i,x}\tilde{M}_{ij} - h_x\psi_i\tilde{D}_{ji}\Big) - b_x\psi_i\tilde{B}_{ji} = \frac{1}{H_0}hu\tilde{I}_j. \tag{A4b}$$

A.1 Direct derivation of the shallow-water coupling condition

The shallow-water coupling condition (54) can also be obtained directly from the continuous variational formulation (A1). Substituting the relation (12) into (A1), and applying the coordinate transformation (15), the expression becomes

$$\begin{aligned} &\left\{\delta\check{\phi}\int_b^{b+h}\phi_x\,\mathrm{d}z\right\}\Big|_{x=x_c} - \left\{\delta\check{\phi}\big(h\,\check{\phi}_x\big)\right\}\Big|_{x=x_c} \\ \rightarrow\ &\delta\check{\phi}_c\left\{\int_0^{H_0}\left(\frac{L_w}{W}\phi_x - \frac{L_w(zh_x + H_0 b_x)}{Wh}\phi_z\right)\frac{h}{H_0}\,\mathrm{d}z - hu\right\}\Big|_{x=x_c}. \end{aligned} \tag{A5}$$

Since the variation $\delta\check{\phi}_c$ is arbitrary, we obtain

$$\begin{aligned} 0 &= \left\{\int_0^{H_0}\left(\frac{L_w}{W}\psi_{i,x}\tilde{\varphi}_i - \frac{L_w(zh_x + H_0 b_x)}{Wh}\psi_i\,\tilde{\varphi}_{i,z}\right)\frac{h}{H_0}\,\mathrm{d}z - hu\right\}\Big|_{x=x_c} \\ &= \left\{\frac{1}{\Upsilon}h\psi_{i,x}\int_0^{H_0}\tilde{\varphi}_i\,\mathrm{d}z - \frac{1}{\Upsilon}h_x\psi_i\int_0^{H_0}z\frac{\mathrm{d}\tilde{\varphi}_i}{\mathrm{d}z}\,\mathrm{d}z - \frac{1}{\Upsilon}H_0 b_x\psi_i\int_0^{H_0}\frac{\mathrm{d}\tilde{\varphi}_i}{\mathrm{d}z}\,\mathrm{d}z - hu\right\}\Big|_{x=x_c} \\ &= \frac{1}{H_0}\left\{h\psi_{i,x}\tilde{I}_i - h_x\psi_i\tilde{G}_i - H_0 b_x(\psi_1 - \psi_{n_z+1})\right\}\Big|_{x=x_c} - \{hu\}|_{x=x_c}, \end{aligned}$$

which is consistent with the coupling condition (54) derived in the main text.

Appendix B Wetting and drying method

In this method, the momentum source term is constructed to preserve hydrostatic balance numerically

$$\mathbf{S} = \begin{pmatrix} 0 \\ -gh\check{b}_x \end{pmatrix} = \partial_x \begin{pmatrix} 0 \\ \frac{1}{2}gh^2 \end{pmatrix},$$

so that the hydrostatic state corresponding to a basin at rest is maintained. Integration of $\mathbf{S}$ over cell k leads to the following representation of the discretised source term

$$\mathbf{S}_k = \begin{pmatrix} 0 \\ -\int_{x_{k-1/2}}^{x_{k+1/2}} gh(x,t)\check{b}_x \,\mathrm{d}x \end{pmatrix} = \begin{pmatrix} 0 \\ \frac{1}{2}gh^2_{(k+1/2)^-} - \frac{1}{2}gh^2_{(k-1/2)^+} \end{pmatrix}, \tag{B6}$$

where $h_{(k+1/2)^-}$ and $h_{(k-1/2)^+}$ are locally constructed values that ensure non-negative depth throughout Ω_S, defined as

$$h_{(k+1/2)^-} = \max\{h_k + \check{b}_k - \check{b}_{k+1/2}, 0\}, h_{(k-1/2)^+} = \max\{h_k + \check{b}_k - \check{b}_{k-1/2}, 0\}, \tag{B7a}$$

with the local beach topography evaluated at the cell interface as

$$\check{b}_{k+1/2} = \max\{\check{b}_k, \check{b}_{k+1}\}, \quad \check{b}_{k-1/2} = \max\{\check{b}_{k-1}, \check{b}_k\}, \tag{B7b}$$

and $\check{b}_k$ the discrete beach topography in (31). Finally, the discretised form of the system, suitable for implementation, is obtained by separating the components of (33), yielding the following equations for the evolution of cell-averaged variables:

$$\dot{h}_k(t) = -\frac{1}{\Delta x_S}\left(F^h_{k+1/2}(t) - F^h_{k-1/2}(t)\right), \tag{B8a}$$

$$(\dot{hu})_k(t) = -\frac{1}{\Delta x_S}\left(F^{hu}_{k+1/2}(t) - F^{hu}_{k-1/2}(t)\right) + \frac{1}{\Delta x_S}S^{hu}_k, \tag{B8b}$$

where $F^h_{k\pm 1/2}$ and $F^{hu}_{k\pm 1/2}$ are the components of the numerical flux $\mathbf{F}_{k\pm 1/2}$ in (34), and S^{hu}_k is the second component of the source term $\mathbf{S}_k$ in (B6).

Acknowledgements OB keenly acknowledges that the late Professor Howell Peregrine had suggested to couple potential-flow and shallow-water solvers at the beach in the late nineties. The project developed using variational tools via several of OB's projects into the presented work, as reported in [5, 7, 19, 21].

Author Contributions Author contributions: FG developed the version in [5, 24]. YL made mathematical and algorithmic corrections, improved associated codes including significant speed-up, reworked the original algorithm, and write-up into presented and implemented weak formulations. OB improved the waterline analysis, tested the software, as well as reproduced the results, and made the GitHub site. MAK, OB, and TB arranged the EU funding, and acted as supervisors. All authors contributed to the writing of manuscript.

Funding This work was funded by the European Union Marie Curie actions as part of "SurfsUp: freak waves and breaking-wave impact on offshore structures" (GA 607596), for FG, and "EAGRE: high-seas wave-impact modelling" (GA 859983) for YL, both projects European Industry Doctorate (EU EID) collaborations between the Maritime Research Institute of Netherlands (MARIN) and the University of Leeds.

Data Availability Codes are found at https://github.com/obokhove/EagreEUEID20202023 (in "couPledbeachwave"). We also aim to make a Zenodo-repository at a later stage.

Declarations

Conflict of interest The authors declare no conflict of interest.

References

1. Haver S (2004) A possible freak wave event measured at the Draupner Jacket January 1 1995. In: Proceedings of rogue waves. pp 1–8
2. Bitner-Gregersen EM, Gramstad O (2016) Rogue waves: impact on ships and offshore structures. Technical report, DNV GL Strategic Research & Innovation position paper 05–2015
3. Bitner-Gregersen EM, Toffoli A (2015) Wave steepness and rogue waves in the changing climate in the North Atlantic. In: Proceedings of the ASME 2015 34th international conference on ocean, offshore and arctic engineering. International conference on offshore mechanics and arctic engineering: structures, safety and reliability, vol 3, pp 003–02024
4. Bitner-Gregersen EM, Vanem E, Gramstad O, Hørte T, Aarnes OJ, Reistad M, Breivik MAK, Natvig B (2018) Climate change and safe design of ship structures. Ocean Eng 149:226–237
5. Gidel F (2018) Variational water-wave models and pyramidal freak waves. PhD thesis, University of Leeds
6. Gidel F, Lu Y, Bokhove O, Kelmanson M (2022) Variational and numerical modelling strategies for cost-effective simulations of driven free-surface waves. https://eartharxiv.org/repository/view/3411/
7. Lu Y (2025) Numerical wavetanks for wave generation, interaction, and dissipation: variational and computational modelling. PhD thesis, University of Leeds. https://etheses.whiterose.ac.uk/id/eprint/37486/
8. Choi J, Kalogirou A, Lu Y, Bokhove O, Kelmanson M (2024) A study of extreme water waves using a hierarchy of models based on potential-flow theory. Water Waves 4:139–179
9. Weller HG, Tabor G (1998) A tensorial approach to computational continuum mechanics using object-oriented techniques. Comput Phys 12:620
10. Jacobsen NG, Fuhrman DR, Fredsøe J (2012) A wave generation toolbox for the open-source CFD library: OpenFoam ®. Int J Numer Meth Fluids 70:1073–1088
11. Perić R, Abdel-Maksoud M (2016) Reliable damping of free-surface waves in numerical simulations. Ship Technol Res 63(1):1–13
12. Perić R, Abdel-Maksoud M (2018) Analytical prediction of reflection coefficients for wave absorbing layers in flow simulations of regular free-surface waves. Ocean Eng 147:132–147
13. Düz B, Huijsmans RHM, Veldman AEP, Borsboom MJA, Wellens PR (2013) An absorbing boundary condition for regular and irregular wave simulations. In: Eça L, Nate EO, García-Espinosa J, Bergan P, Kvamsdal T (eds) MARINE 2011, IV international conference on computational methods in marine engineering. Springer, Barcelona

14. Higdon RL (1986) Absorbing boundary conditions for difference approximations to the multidimensional wave equation. Math Comput 47:437–459
15. Higdon RL (1987) Numerical absorbing boundary conditions for the wave equation. Math Comput 49:65–90
16. Düz B, Borsboom MJA, Veldman AEP, Wellens PR, Huijsmans RHM (2017) An absorbing boundary condition for free surface water waves. Comput Fluids 156:562–578 (**Ninth international conference on computational fluid dynamics (ICCFD9)**)
17. Smit P, Zijlema M, Stelling G (2013) Depth-induced wave breaking in a non-hydrostatic, near-shore wave model. Coast Eng 76:1–16
18. Wang W, Pakozdi C, Kamath A, Bihs H (2021) A fully nonlinear potential flow wave modelling procedure for simulations of offshore sea states with various wave breaking scenarios. Appl Ocean Res 117:102898
19. Kristina W, Bokhove O, Groesen EWC (2014) Effective coastal boundary conditions for tsunami wave run-up over sloping bathymetry. Nonl Proc Geophys 1:317–369
20. Audusse E, Bouchut F, Bristeau MO, Klein R, Perthame B (2004) A fast and stable well-balanced scheme with hydrostatic reconstruction for shallow water flows. SIAM J Sci Comput 25:2050–2065
21. Klaver F (2009) Coupling of numerical models for deep and shallow water. Master's thesis, University of Twente, Netherlands
22. Luke JC (1967) A variational principle for a fluid with a free surface. J Fluid Mech 27:395–397
23. Engsig-Karup AP, Bingham HB, Lindberg O (2009) An efficient flexible-order model for 3d nonlinear water waves. J Comput Phys 228(6):2100–2118
24. Bokhove O (2022) Variational water-wave modeling: from deep water to beaches. In: The mathematics of marine modelling. Springer, Cham. pp 103–134
25. Gagarina E, Vegt J, Bokhove O (2013) Horizontal circulation and jumps in Hamiltonian wave models. Nonlinear Proc Geophys 20:483–500
26. Harten A, Lax PD, Leer BV (1983) On upstream differencing and Godunov-type schemes for hyperbolic conservation laws. SIAM Rev 25:35–61
27. Toro FE (2009) Riemann solvers and numerical methods for fluid dynamics. Springer, Berlin
28. Hairer E, Lubich C, Wanner G (2006) Geometric numerical integration. Springer, Berlin
29. Choi J, Kalogirou A, Lu Y, Bokhove O, Kelmanson M (2024) A study of extreme water waves using a hierarchy of models based on potential-flow theory. Water Waves 4:139–179
30. Rathgeber F et al (2016) Firedrake: automating the finite element method by composing abstractions. ACM Trans Math Softw 43:1–24
31. Ham DA et al (2023) Firedrake user manual, 1st edn. Imperial College London, London
32. Cotter C, Bokhove O (2010) Variational water-wave model with accurate dispersion and vertical vorticity. J Eng Math 67:33–54
33. Firedrake: Solving PDEs. http://www.firedrakeproject.org/solving-interface.html#preconditioning-mixed-finite-element-systems